University of Crete
Department of Physics

– Bachelor's Thesis –

Submitted in partial fulfillment of the requirements for the degree of Bachelor of Science in Physics

---

A systematic meta-analysis of physical parameters of Galactic supernova remnants

---

Author:
Issa Hussein-Bassia

Instructors:
Prof. Andreas Zezas
Dr. Ioanna Leonidaki
Dr. Maria Kopsacheili

Heraklion, October 2023

Contents

I | Preamble

Abstract

Supernova remnants (SNRs) are the aftermath of massive stellar explosions, representing critical phases in the life cycle of stars and playing an important role in galactic evolution. This study delves into the properties and evolution of Galactic SNRs through a comprehensive statistical analysis of shock velocity, electron density and age data. Our study provides, for the first time, a picture of the statistics of 62 Galactic SNRs both as a population and as regions within individual objects and offers insights into their diverse properties and evolutionary paths. Diverse shock velocity data (including upper and lower limits) and the ages of the SNRs, processed using a Monte Carlo sampling approach, are compared with the theoretical evolution model of Cioffi et al. We find good agreement between the data and the model. Analysis of electron density and shock velocity distributions for the entire sample of SNRs shows that they are consistent with a log-normal distribution and a skewed log-normal distribution, respectively. Within individual remnants, our study reveals that electron density and shock velocity show larger scatter in younger objects, reflecting the varying conditions of the ambient medium immediately surrounding the explosion epicenter and their impact on SNR evolution.

Acknowledgments

I want to thank professor Stavros Litsas who was the first to see my potential and encourage me to follow my dreams. I want to thank my parents for continually supporting all my decisions and helping me financially, who, despite our occasional disagreements, did so much better than their parents.

Next, I'd like to thank Dr. Maria Kopsacheili for those hilarious times at Skinakas and for essentially pulling the lever for my involvement in this project. And, last but certainly not least, Dr. Ioanna Leonidaki and professor Andreas Zezas for their unwavering support, guidance and patience with me in this momentous opportunity.

II | Main Matter

1 | Introduction

Supernova explosions are one of the most interesting and energetic phenomena observed in the universe. These explosive events signify the dramatic conclusion of a massive star's life cycle, unleashing enormous amounts of energy. During a supernova explosion, a shock wave is produced, propelling stellar content outward into the interstellar medium (ISM) at supersonic speeds. This violent ejection causes the ISM to condense and heat up, resulting in the emission of radiation across a significant portion of the electromagnetic spectrum. The bright shell-like structure that remains, extending outward from the original location of the star, is appropriately termed a supernova *remnant*. Observing and studying supernova remnants provides valuable insights into the life cycles of massive stars, the dynamics of interstellar matter, and the processes responsible for cosmic nucleosynthesis. They also serve as laboratories for understanding shock physics, particle acceleration, and magnetic field amplification in extreme environments.

1.1 Classification of Supernovae

Supernovae are classified by the appearance or absence of specific emission lines (hydrogen, helium and silicon) in their spectra as well as the morphology of their light curves. They can be broadly categorized into two main types. Type I supernovae are distinguished by the absence of hydrogen lines in their spectra, while Type II supernovae feature the presence of these hydrogen lines. Furthermore, each of these main types can be classified into further subtypes, which are described below. All types, apart from Ia, come from the core collapse of massive stars. As these stars exhaust their nuclear fuel, the core contracts and eventually reaches a point where it can no longer withstand its own gravity, leading to a sudden collapse and a catastrophic explosion which rips the star apart.

Type Ia

Type Ia supernovae are characterized by the absence of hydrogen lines and the appearance of helium and silicon lines in their spectra. They occur in binary star systems where one of the stars is a white dwarf and the companion star can be anything from a giant star to an even smaller white dwarf. The white dwarf accretes mass from its companion until it reaches a critical mass (the Chandrasekhar limit), beyond which it cannot support its own gravity. This triggers rapid nuclear fusion of carbon and oxygen, leading to a runaway thermonuclear explosion.

Type Ib

Type Ib supernovae are similar to Type Ia supernovae, but they lack silicon lines in their spectra. They are believed to occur when a massive star loses its outer hydrogen envelope through stellar winds or interactions with a companion star, leaving behind a helium-rich core that undergoes a core-collapse.

Type Ic

Type Ic supernovae lack all hydrogen, helium and silicon lines in their spectra. Like Type Ib, they likely result from the loss of their outer envelopes, leaving behind a bare core of heavier elements, such as carbon and oxygen.

Type IIb

These are transitional supernovae that initially display hydrogen lines (like Type II) but later lose their hydrogen lines and show evidence of helium lines, resulting in a Type Ib supernova.

Type II-P (Plateau)

These supernovae show a plateau phase in their light curves, where the luminosity remains relatively constant for a period before declining.

Type II-L (Linear)

Type II-L supernovae do not display the plateau phase, and their light curves follow a linear decline.

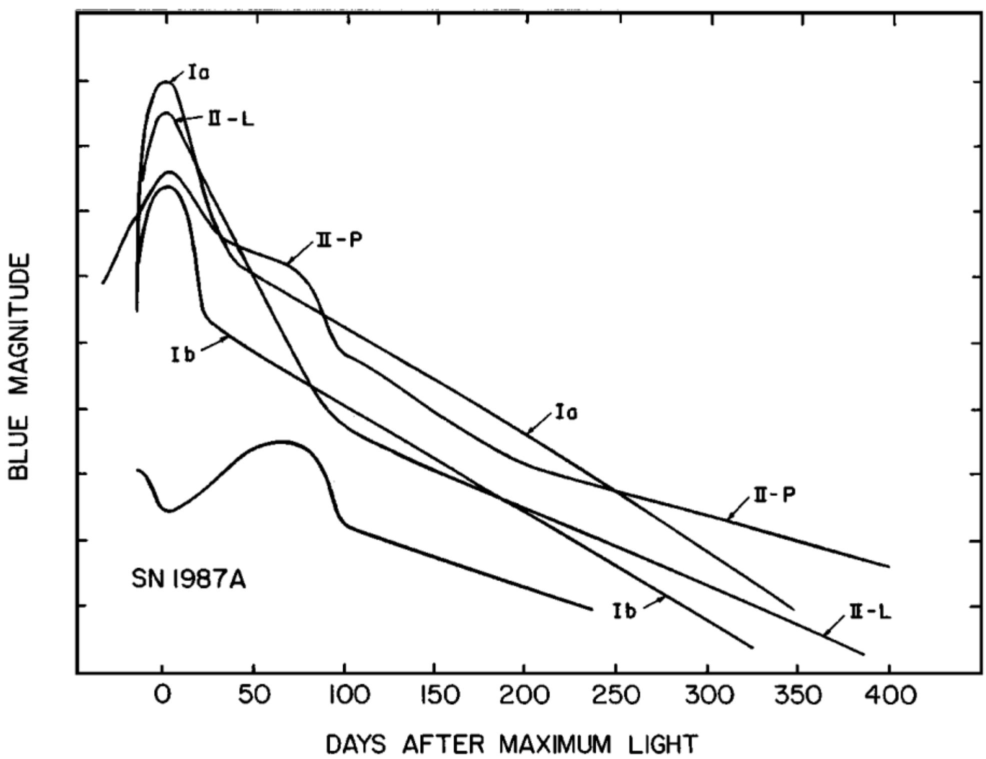

Figure 1.1: Light curves of different types of supernovae. Figure taken from Filippenko (1997) [40].

1.2 What is a Supernova Remnant?

When a massive star reaches the end of its life cycle or, a white dwarf in a binary system accretes enough mass from its moderately massive companion until it is no longer able to withstand its own gravitational pull, it undergoes a catastrophic collapse, leading to an incredibly powerful and luminous explosion. This explosion expels the star's outer layers into the surrounding space at extremely high velocities. The ejected material, consisting of newly synthesized elements, interacts with the ISM and creates a shockwave that propagates outward from the explosion's epicenter.

As the shockwave expands, it sweeps up and compresses the surrounding ISM, leading to the formation of a shock front that is seen as a bright shell of hot gas. This shell of shocked material as well as the material it contains is what we refer to as a supernova remnant (SNR). SNRs can span tens to hundreds of light years in size and emit radiation across the electromagnetic spectrum through various emission mechanisms as well as high energy particles.

1.2.1 Structure

SNRs consist of a multi-layered composition characterized by distinct regions that play integral roles in the evolution of the remnant as well as its interactions with the surrounding interstellar medium. At the core lies the compact, highly energetic neutron star or black hole resulting from the stellar core collapse. In the case of Type Ia supernovae no compact object is left behind. The runaway thermonuclear explosion unbinds the star entirely. If a neutron star is left behind, it often emits intense radiation, powering the entire SNR. Surrounding this central region is the innermost layer composed of high-velocity ejecta, comprising heavy elements synthesized within the stellar core during its fusion processes. When these ejecta encounter the ambient medium, they form clumps and filaments such as those seen in Fig. 1.2.

Moving outward, the intermediate layer represents the reverse shock. As the explosion blast wave sweeps up mass in a forward shock, the latter decelerates, allowing for supernova ejecta to catch up and for a reverse shock to be formed. This reverse shock heats the supernova ejecta as it loses energy and decelerates. Reverse shocks also form when ejecta encounter the slower-moving material expelled from the progenitor star as a stellar wind during its life. Reverse shocks contribute to the formation of filaments.

The outermost layer, known as the forward shock, marks the interface between the SNR and the surrounding ISM. This shock front is associated with particle acceleration to high energies and production of strong emission across the electromagnetic spectrum. The departure from uniformity of the shape of many SNRs is attributed to the distribution of the ISM density, including the presence or absence of HII regions or other objects (e.g. molecular clouds) contributing to the ambient density.

1.2.2 Types of SNRs

Based on their morphology, there are three types of SNRs:

- **Shell-type** remnants, as their name suggests, emit most of their radiation from a shell of shocked material. We view this as a bright ring, since when we look at the edges of the three-dimensional shell, there is more shocked material along our line of sight than if we look elsewhere in the shell. This is known as limb brightening.

Figure 1.2: Visual structure of supernova remnants. *From left to right*: The Medusa Nebula in the constellation of Gemini, Simeis 147 in the constellation of Taurus, and the Crab Nebula in the same constellation. The first two images were taken at the Skinakas Observatory and the last one from Hester (2008) [53].

- **Plerions** or **pulsar wind nebulae** (PWN) are powered by a pulsar located at their centre and, in constrast to shell-type remnants, they emit most of their radiation from within the expanding shell. This means that they appear as a filled region of emission rather than a ring of emission.

- **Composite** remnants are a cross between the other two remnant types, and appear either shell-like or plerion-like, depending on the wavelength of the observations. In general, thermal composites appear shell-like at radio wavelengths and plerion-like in X-rays, while plerionic composites appear plerion-like at both radio and X-ray wavelengths, but also show shell structures. Another major difference between plerionic and thermal composites is the radiation mechanism. In plerionic composites the emission from the center is non-thermal (radio, X-rays, optical) while in thermal composites the X-ray emission is thermal.

Based on their spectral characteristics, there are two more types of SNRs:

- **Balmer dominated** remnants, are determined based on the intense hydrogen Balmer lines and weak or absent forbidden lines of [O III], [S II] and [N II] in the optical band. The intense emission from Balmer lines arises from the neutral hydrogen of the surrounding ISM that is being swept up and ionized by the SNR's shock wave. These types of remnants are thought to originate from Type Ia supernovae, which, unlike Type II (core-collapse) supernovae, do not produce enough energy to ionize large volumes of surrounding ISM, leaving most hydrogen in its neutral form, to be ionized by the shock wave.

- **Oxygen-rich** remnants, are determined based on the intense emission of forbidden oxygen lines (e.g. [O III]) in the optical band as well as X-rays. They are believed to originate from Type Ib supernovae, where massive stars lose their outer hydrogen envelopes through intense stellar winds right before exploding. This is why these supernova remnants display absence of hydrogen lines and abundance in oxygen that originates from the interior of the star.

1.2.3 Evolution of SNRs

Throughout its evolution, an SNR goes through four different phases.

1. Initially, the SNR is in the **free expansion** phase, where the blast wave from the explosion overtakes the rapidly expanding ejected material and sweeps up and compresses the surrounding interstellar or circumstellar medium creating a shock front. In this phase the mass of the swept up material is much less than the mass of the ejecta and the shell's expansion velocity remains constant. Assuming a uniform ambient medium, this phase typically lasts a few hundred years and in that time the SNR reaches a radius of a few parsecs.

2. As the SNR interacts with this ambient medium, it eventually enters the **adiabatic** or **Sedov-Taylor** phase. In this phase the mass of the material swept up by the blast wave becomes larger than the mass of the ejecta and the dynamics are described by the adiabatic blast wave similarity solution of Taylor and Sedov, which is determined by the total mass of expanding gas (mostly swept up interstellar or circumstellar gas) and the energy released in the initial explosion. Radiative losses are unimportant in this phase; there is no exchange of heat with the surroundings (hence the term *adiabatic*). However, in earlier phases such as this, as the shock wave starts to decelerate and transfer enormous amounts of kinetic energy to the swept up material, it heats it up to millions of degrees, enabling it to emit intense X-rays, cosmic rays and synchrotron radiation among other wavelengths. This shell continues to grow as the shock wave progresses outward. This phase typically lasts a few thousand years and the shell reaches a radius of a few tens of parsecs in this time.

3. Subsequently, the remnant transitions into the **radiative** phase. In this phase, as the shell continues to decelerate and lose its kinetic energy, thermal radiation losses become significant. The SNR begins to cool down to a few tens of thousands of degrees, allowing for optical emission to arise. This phase typically lasts a few hundred thousand years and during that time the SNR's radius increases a few more tens of parsecs.

4. Finally, over time, the object loses its identity as an SNR as it dissipates its energy and merges with the interstellar medium, enriching it with heavy elements and providing a fertile environment for the formation of new stars. This is known as the **dissipation** or **fade-out** phase.

During these phases, which are also shown in Fig. 1.3, the SNR gradually loses its initial kinetic energy and begins to cool and fade, interacting with its surroundings and enriching the ISM with heavy elements and energy. These remnants play a crucial role in the evolution of galaxies by recycling stellar material and influencing the formation of new stars and planetary systems. Understanding the evolution of SNRs is therefore crucial for comprehending the complex interplay between stellar life cycles and galactic ecosystems, making it a fundamental area of research in astrophysics and cosmology.

Cioffi et al. [23] have developed a model for the evolution of SNRs. Since in this work we are interested in the optical emission of SNRs, we focus on the adiabatic and radiative phases of the model, as most SNRs that emit in optical wavelengths are in either of those two phases. We will later use this model to study the relation between the shock velocity and age of SNRs. According to Cioffi et al., the transition from the Sedov-Taylor to the

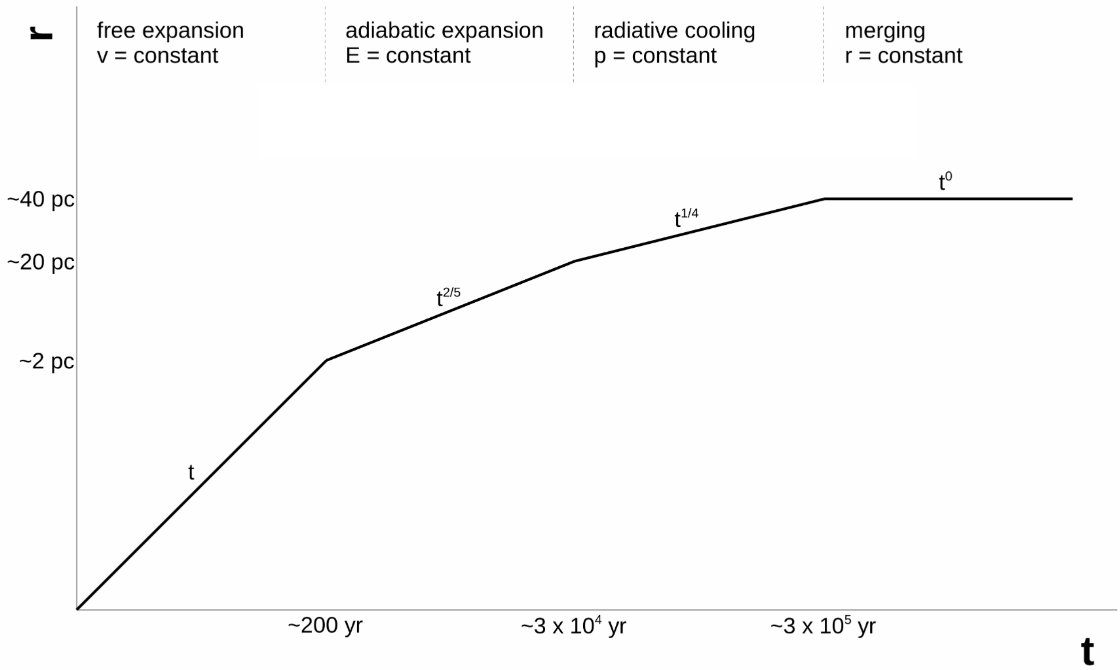

Figure 1.3: The plot shows the radius of the SNR as a function of time, indicating characteristic timescales for the different phases of SNR evolution. The final phase refers to the merging of the SNR with the ISM and its subsequent dissipation, what we call fade-out phase in this work. Figure taken from Arribas et al. (2017) [86].

radiative phase takes place near the shell-formation time t_{sf}, when the temperature of the first element of gas becomes zero. In this case

$$t_{sf} = 3.61 \times 10^4 \frac{E_{51}^{3/14}}{\zeta_m^{5/14} n^{4/7}}\, yr, \tag{1.1}$$

where $E_{51} = E_0(erg)/10^{51}$ is the total energy of the explosion in units of 10^{51} erg, $n(cm^{-3})$ is the pre-shock density, and ζ_m is the metallicity factor which is 1 for solar abundances. Hence, the transition time is given by the relation:

$$t_{tr} = \frac{t_{sf}}{e}\, yr \tag{1.2}$$

where e is the base of the natural logarithm.

The shock velocity in each of these two phases as a function of the pre-shock density n and the SNR age t are given by:

$$\nu_{ST} = 0.4(\xi 10^{51} E_{51})^{1/5} \rho^{-1/5} (3.3 \times 10^7 t(yrs))^{-3/5}\, km\, s^{-1} \tag{1.3}$$

for the adiabatic phase, and:

$$\nu_{rad}(n,t) = \nu_{tr}(n)\left(\frac{4t}{3t_{tr}(n)} - \frac{1}{3}\right)^{-7/10} km\, s^{-1} \tag{1.4}$$

for the radiative phase, where

$$\nu_{tr}(n) = 413 n^{1/7} \zeta_m^{3/14} E_{51}^{1/14}\, km\, s^{-1} \tag{1.5}$$

is the velocity at the beginning of the radiative phase. In the above relations, $\xi = 2.026$ a numerical constant, ζ_m is the metallicity factor as mentioned earlier, $\rho = \mu_H n m_H = 2.3 \times 10^{-24}\, gr\, cm^{-3}$ the total mass density, μ_H the mean mass per hydrogen nucleus, and m_H the hydrogen-atom mass.

1.3 Information from Optical Spectra

Optical emission from SNRs arises from radiative cooling of shocked gas. SNR spectra reveal the chemical composition of the ejecta and the surrounding ISM as well as their excitation state. More specifically, they show strong emission lines from a variety of ionization states, including H I, [O II], [O III], [S II] and [N II] as well as weaker emission lines from ions such as He I, He II, [O I], [N I], [Ne III], [Fe II], [Fe III], [Ca II] and [Ar III] (Fesen et al., 1985) [32]. Optical emission lines can be used as diagnostic tools, firstly for the detection and identification of SNRs and, secondly, for the extraction of useful information for these objects, such as their temperature, electron density, metallicity and shock velocity.

Electron Temperature

Temperature can be calculated from the intensity ratio of specific emission lines. Appropriate lines are those of the same ion which arise from collisionally excited states of considerable energy difference. It is clear that the excitation rates and, therefore, the intensities of the corresponding emission lines will depend strongly on temperature. Consequently, the intensities of emission lines arising from these states can be used to calculate electron temperature as shown in Fig. 1.4. Some of these ions are [O III], [N II], [Ne III] and [S III].

Shock Velocity

Knowing the electron temperature of the SNR, we can estimate the velocity of the shock waves. The velocity and strength of the shock waves in SNRs is reflected in the temperature-sensitive emission line of [O III] at 5007 Å. The greater the shock velocity, the greater the electron temperature of the medium behind the shock front, which, in turn, results in a more prominent emission of the temperature-sensitive [O III] line. It has been observed that the absence of the [O III] line from SNR spectra is associated with shock waves < 100 km s^{-1} (Hartigan et al., 1987) [51]. The immediate deduction of shock velocity from the [O III] line is challenging as other parameters, such as density, magnetic field strength, ionization state and metallicity also affect shock velocity. However, there are models (Baldwin et al., 1981 [4] & Allen et al., 2008 [2]) which take these parameters into account and are able to estimate shock velocities in SNRs based on the [O III] emission line. Across the publications we considered in this study, shock velocity measurements were obtained using mostly three methods among a few other, less common ones. These include the one just described as well as:

1. **Doppler shift**. We recognize the emission lines that we observe in spectra and from their wavelength shift, we are able to estimate the velocity at which the gas emitting these lines is moving. Therefore, obtaining spectra from the shock front allows us to measure its velocity using this method. However, it should be noted that this method gives only the radial velocity component.

2. **Emission line broadening**. The hotter the emitting medium, the greater the line broadening observed in its spectra. Line broadening allows us to estimate the temperature in shock fronts, which is related to the velocity at which the gas is expanding. There are models that relate the shock temperature to its velocity, similar to those described earlier.

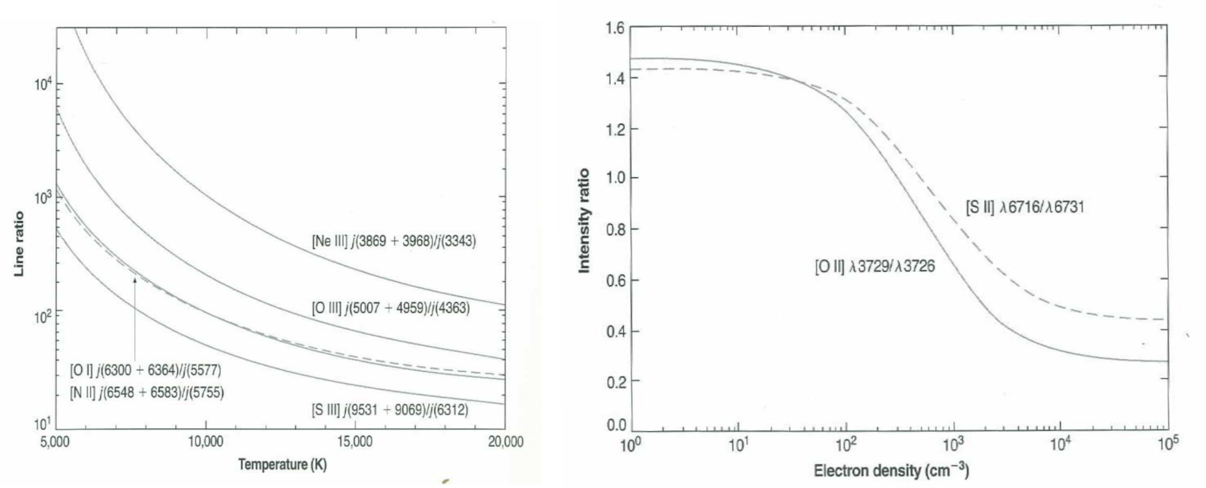

Figure 1.4: Electron temperature and density diagnostics. *Left*: Electron temperature as a function of the intensity ratio of various forbidden emission lines. The plot refers to an electron density of $n_e = 1$ cm^{-3}. *Right*: Electron density as functions of intensity ratios of [O II]λ3729/3726 and [S II]λ6716/6731. The plot refers to a temperature of $T = 10^4$ K. For other temperatures, the curves are approximately correct if the x-axis is scaled according to $n_e(10^4/\mathrm{T})^{1/2}$. Figures taken from Osterbrock & Ferland (2006) [84].

Electron Density

The mean electron density can be calculated from observing the outcomes of collisional excitation. This is possible by comparing the intensities of two forbidden emission lines of the same ion, emitted from slighlty different energy states (small energy difference between the states). The most common examples of ions used to measure electron density are those of oxygen [O II]λ3729/3726 and sulfur [S II]λ6716/6731. These emission line pairs are very close to each other, energetically speaking, which gives them approximately the same probability to be occupied by collisionally excited electrons. The intensity of the emission resulting from these two levels is driven by two main factors. One is the statistical weight, that is how many electrons each level can occupy. This plays a role in the intensity of the lines: the greater the number of electrons occupying the energy level, the greater the number of photons that can potentially be emitted by spontaneous de-excitation. The other is the lifetime of electrons at these levels, i.e. the time an electron spends at this level before spontaneously de-exciting at the ground state, emitting a photon of analogous wavelength. The energy state with the longer lifetime is more vulnerable to higher densities (where collisional de-excitations are increased), therefore it will have different de-excitation rates compared to the energy state with the smaller lifetime. Therefore, the relative population of electrons in these energy states and, subsequently, the intensity of the corresponding emission lines depends on electron density, which controls the number of collisional de-excitations and, subsequently, the number of spontaneous de-excitations, i.e. emissions of photons, that occur. Osterbrock & Ferland (2006) [84] have constructed models that take these dynamics (and those described earlier in *Electron Temperature*) into account and can be used to estimate electron density (and temperature) from intensity ratios of various emission lines. Examples of their work are shown in Figure 1.4.

1.4 Motivation

So far, there has not been any systematic analysis on SNR properties. However, thanks to a large body of works presenting information on individual objects or regions within them, we are able to perform a systematic meta-analysis of these data in order to obtain a picture of the SNRs properties (e.g. shock velocity and density). In this study, we will be focusing on SNRs emitting radiation in the visible part of the electromagnetic spectrum. SNRs emitting such radiation are typically at the end of their adiabatic phase or within their radiative phase of evolution, as described earlier. We will, for the first time, quantify the variability of the physical parameters within these celestial objects and present the correlation between their shock velocities, electron densities and ages. Additionally, by analyzing data from numerous remnants of varying ages, we will investigate their evolutionary patterns and compare them to the theoretical model of Cioffi et al., hoping to mature our understanding of these extraordinary phenomena.

2| Sample Selection

2.1 Sample Selection & Dataset Construction

Our literature survey is based on the Galactic SNR catalogue of Green (2022) [48]. We thoroughly examined all available publications of the entire SNR sample, with specific emphasis on observations conducted within the optical waveband, focusing on measurements of the remnants' shock or expansion velocities, densities and temperatures, based on a variety of methods and tracers. Among the 294 SNRs listed in Green's catalogue at the beginning of this project, we ended up focusing on 62 (21%) that possessed documented data derived from optical observations. For the remaining objects there is either no information on their optical emission or no information on their physical properties.

To aid our data mining process, we created a Python script that searched for tracers within the abstracts of the publications and retained the ones with at least one of the tracers we looked for. These tracers included spectroscopic observations in the optical band or optical emission line ratios (e.g. [N II]/Hα, [S II]/Hα, [O III]/Hβ, etc. due to their significance as temperature, density and shock velocity diagnostics), keywords associated with optical emission, such as 'H-alpha', 'Balmer' and 'optical', and measurements of physical parameters, namely shock velocity, electron density and temperature. Certainly, there is a chance that a paper presents measurements of physical parameters in the body of the text and the tracer is not listed in the abstract. However, from examining a small number of publications not retained by our script, we are confident that the search was adequately exhaustive.

After applying this filtering process, we conducted a manual search within the remaining publications to identify these tracers in the body of the text, and we carefully documented any valuable information we found. If measurements of physical properties were reported, we ensured that the values of a property (e.g. velocity) were measured in the same regions of SNRs or using the same method. To facilitate a comprehensive analysis, we then aggregated the data extracted from these publications into a consolidated dataset.

Age and distance information was obtained from the database of high-energy observations of Galactic SNRs (Ferrand & Safi-Harb, 2012) [29]. Our final sample of optically-selected SNRs that made it to our dataset along with the number of publications from optical observations kept for each object is presented in Table 2.1. Our dataset not only allowed for a unified analysis of the available measurements but also enabled us to explore the correlations between the physical parameters of SNRs (such as velocity and density) as a function of their age, providing for the first time a picture of the overall trends of the properties of the SNR population within our Galaxy. While temperature data were also obtained, they were not enough to draw any reliable conclusions on their relationship to other parameters.

Table 2.1: Basic properties of the SNRs used in our study. The number of publications from optical observations per remnant used in this work are also shown. Multiple age and distance estimates are given from different studies and measurement methods used.

No.	SNR	Name(s)	Age (yrs)	Distance (kpc)	No. of Publications
1	G4.5+6.8	Kepler	416	2.9±0.4	2
2	G6.4-0.1	W28	33000-36000	2, 1.8-3.55	2
3	G13.3-1.3	G13.3-1.3	-	3.3±1.3	1
4	G15.1-1.6	G15.1-1.6	-	2.1-2.2	1
5	G17.4-2.3	G17.4-2.3	-	-	1
6	G32.8-0.1	Kes 78	5700-22000	6-8.5	1
7	G34.7-0.4	W44	6400-7500	2.1-3.3, 2.5	2
8	G38.7-1.3	G38.7 -1.3	3800-14700	-	1
9	G39.7-2.0	W50	30000-100000, 18000-210000	5, 2-6	2
10	G49.2-0.7	W51C	∼30000	∼6	5
11	G53.6-2.2	3C 400.2	15000-50700, 110000	6.7±0.6, 6.7-7.8	1
12	G54.4-0.3	HC40	61000	3	1
13	G59.5+0.1	G59.5+0.1	-	11	1
14	G59.8+1.2	G59.8+1.2	-	-	1
15	G64.5+0.9	G64.5+0.9	-	∼11	5
16	G65.3+5.7	G65.3+5.7	20000-30000	≈1.2, 0.6-1.5, 1	1
17	G66.0-0.0	G66.0-0.0	-	2.3-3.96	1
18	G67.6+0.9	G67.6+0.9	-	-	2
19	G67.7+1.8	G67.7+1.8	1500-13000	7-17, 16.7	1
20	G67.8+0.5	G67.8+0.5	-	-	4
21	G69.0+2.7	CTB 80	∼10000, 60000, 30000	2.5, 1.5-4.6	2
22	G70.0-21.5	G70.0-21.5	-	1-2	1
23	G73.9+0.9	G73.9+0.9	11000-12000	-	7
24	G74.0-8.5	Cygnus Loop	18000, ∼10000	∼0.89	3
25	G78.2+2.1	DR4, γ Cygni SNR	8000-16000, ∼7000	-	2
26	G82.2+5.3	W63	13500-26700	1.6-3.3	1
27	G85.9-0.6	G85.9-0.6	6400-49000	5	1
28	G89.0+4.7	HB21	4800-18000	0.8-1.7	2
29	G109.1-1.0	CTB 109	8800-14000, 9000-9200	3.6-5.2, 3.1±0.2	1
30	G111.7-2.1	Cas A	340	3.3±0.1, 3.4	3
31	G114.3+0.3	G114.3+0.3	∼41000	2-3	1
32	G116.5+1.1	G116.5+1.1	15000-50000	∼3	3
33	G116.9+0.2	CTB 1	7500-18100, 7500-11000, 16000	1-4.7, 0.9-4.7, 2-3.5	2
34	G119.5+10.2	CTA 1	13000	1.4, 1.1-1.7	2
35	G120.1+1.4	Tycho	451	-	2
36	G126.2+1.6	G126.2+1.6	270000	4.5, 2-5	2
37	G130.7+3.1	3C58	839	2.6±0.2	2
38	G132.7+1.3	HB3	25000-72000	2-2.2	2
39	G156.2+5.7	G156.2+5.7	7000-36600, 20000	0.68-3, 1.7	1
40	G159.6+7.3	G159.6+7.3	-	<2.5	2
41	G166.0+4.3	VRO 42.05.01	9000-20100, 60000	2-3.6	1
42	G179.0+2.6	G179.0+2.6	>10000	∼3.5	3
43	G180.0-1.7	S147	26000-34000	0.8-0.9, 0.6-1.9	2
44	G184.6-5.8	Crab Nebula	966	-	2
45	G189.1+3.0	IC443, 3C157	9000, ∼10000	0.5-2.5	2
46	G205.5+0.5	Monoceros Nebula	30000-150000	-	3
47	G206.9+2.3	PKS 0646+06	64000	3-6.5, 1-2.3, ∼2.2	1
48	G213.0-0.6	G213.0-0.6	-	∼2.4	1
49	G260.4-3.4	Puppis A, MSH 08-44	2200-5400	2-4	2
50	G263.9-3.3	Vela	9000-27000	0.25	1
51	G284.3-1.8	MSH 10-53	∼10000, 2930-3050	1-2.9, 3.7-5.4, 6-6.2, 6.2±0.9	3
52	G296.1-0.5	G296.1-0.5	2800-28000	3-5	1
53	G296.5+10.0	Milne 23, PKS 1209-51/52	7000-10000	1.3-3.9	1
54	G299.2-2.9	G299.2-2.9	≈8700	≈5	1
55	G315.1+2.7	G315.1+2.7	-	1.7	1
56	G315.4-2.3	RCW 86, MSH 14-63	2000-12400	2.5±0.5, 2.3±0.2, 3.2	5
57	G320.4-1.2	MSH 15-52, RCW 89	1700-1900	4	1
58	G326.3-1.8	MSH 15-56	9800-16500	3.2	1
59	G327.6+14.6	SN1006, PKS 1459-41	1017	2.1	5
60	G332.4-0.4	RCW 103	2000, 2000-4400, 1200-3200	3.3, 3.2, 2.7-3.3	4
61	G332.5-5.6	G332.5-5.6	7000-12100	2.2-3.8	1
62	G343.0-6.0	RCW 114	∼20000	0.2-1.5	1

3 | Data Analysis

3.1 Handling Special Data Types

Unlike traditional lab data, which often consist of well-behaved values and associated errors, our dataset comprised various data types, each with its unique characteristics and uncertainties. Dealing with this diverse range of data types presented a significant challenge, as we couldn't simply ignore or treat them uniformly. Discarding any of these data would have resulted in a substantial loss of valuable information, which is particularly critical considering our already limited sample and dataset size. It was, therefore, imperative to develop a methodology that effectively incorporated all the available data, allowing us to extract as much information as we could in order to derive meaningful insights and draw reliable conclusions.

A/A	Shock Velocity (km s^{-1})	Data Type
1	>90	Lower limit
2	<110	Upper limit
3	90±20	Value with error
4	90-110	Value range
5	≈100	Approximate value

Table 3.1: Example of different types of indicative shock velocity measurements in a single region of an SNR.

In Table 3.1 we present indicative shock velocity measurements for a single region of an SNR. We would like to obtain a final mean or median value as well as an error estimation for the shock velocity in this region, by combining all available measurements. Because of the different nature of the uncertainties in each indicative measurement we cannot use traditional methods of error propagation. Therefore, to address the complexity of our dataset and achieve this, we adopted a probabilistic approach. More specifically, we used a Monte Carlo sampling method to sample values from relevant distributions. In other words, we draw values from appropriate distributions for each one of the measurements in Table 3.1, depending on their type.

For instance, to handle value ranges, we made a thousand draws from a chosen Gaussian distribution. A Gaussian function is given by the formula:

$$G(x) = Ae^{-\frac{(x-b)^2}{2\sigma^2}}, \tag{3.1}$$

where A is the height of the curve's peak, b the position of the center of the peak and σ the standard deviation.

There's a special relationship between the full width at half maximum (FWHM) of the curve and its standard deviation. The half of the maximum is located at the point where

$G(x) = A/2$. Assuming a Gaussian function centered at zero (i.e. $b = 0$), substituting into equation 3.1 and solving for x yields:

$$x_{FWHM} = \pm\sqrt{2\ln 2}\,\sigma \tag{3.2}$$

The FWHM is then $2\sqrt{2\ln 2}\,\sigma$, and so

$$\sigma = \frac{FWHM}{2\sqrt{2\ln 2}}. \tag{3.3}$$

The center of our chosen Gaussian distribution was set to the midpoint of the value range, and the standard deviation was determined, according to equation 3.3, based on a FWHM that was set equal to the difference of the value range.

To quantify the uncertainty associated with the value range, we derived a representative value using either the mean or the median of the random sample drawn from the distribution and we calculated the error estimation based on its standard deviation.

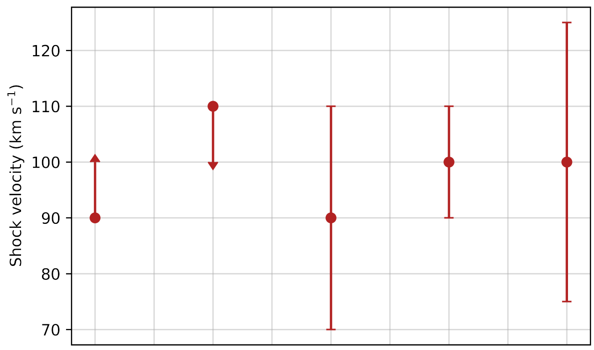

Figure 3.1: Plot representation of the shock velocity measurements in Table 3.1.

Approximate values, where uncertainties are not reported, were handled in a similar way, using a Gaussian distribution centered at the approximate value. To account for the uncertainty associated with an approximate value, we introduced a 25% error. To determine the appropriate standard deviation for this Gaussian, we employed, again, equation 3.3, equating the FWHM to the difference of the value range induced by the 25% error. This choice for sigma ensures that the drawn samples appropriately reflect the approximate value's uncertainty.

To address upper and lower limits, we applied a similar probabilistic method. For lower limits, we employed a Heaviside step function that extends up to five times the lower limit. This step function allowed us to sample from within the specified range, effectively incorporating the constraint while accounting for uncertainties in the data.

To visualise the sampling process, we provide an example. Table 3.1 shows a set of hypothetical shock velocity measurements of various data types in a single region of an SNR and Figure 3.1 their representations on a plot. Value ranges are represented with a central value equal to the average of the upper and lower limits of the range and an error bar corresponding to their half difference. For approximate values a 25% error is introduced. Finally, upper and lower limits are represented with arrows pointing down and up, respectively.

In Figure 3.2 we show histograms of a thousand draws for each measurement. In Figure 3.3, the left panel shows the histograms combined into a single plot, while the right panel combines the draws into a single histogram. We calculate the mean or median value,

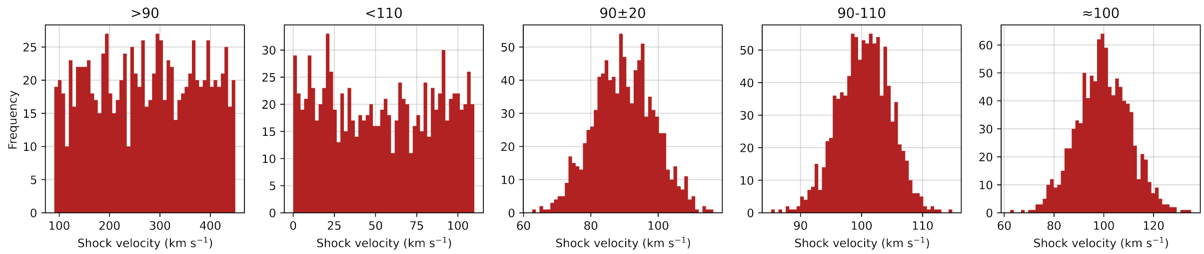

Figure 3.2: Visualisation of the Monte Carlo sampling method used in this work. Each histogram represents a sample of a thousand draws from appropriate distributions relative to the data type of each indicative shock velocity measurement of Table 3.1 which is shown at the top in units of km s^{-1}.

depending on the case, as well as the standard deviation of the combined distribution to get a measurement for this region representing all available information. It's needless to say that in our case, we also had errors and special data types in the x-axis. The process remains the same, only this time it is performed twice.

Overall, this probabilistic methodology allowed us to effectively deal with various types of special data, taking into account their inherent uncertainties and constraints. The approach presented here provides a robust framework for handling and analyzing all available data from complex datasets, enabling more accurate and reliable results.

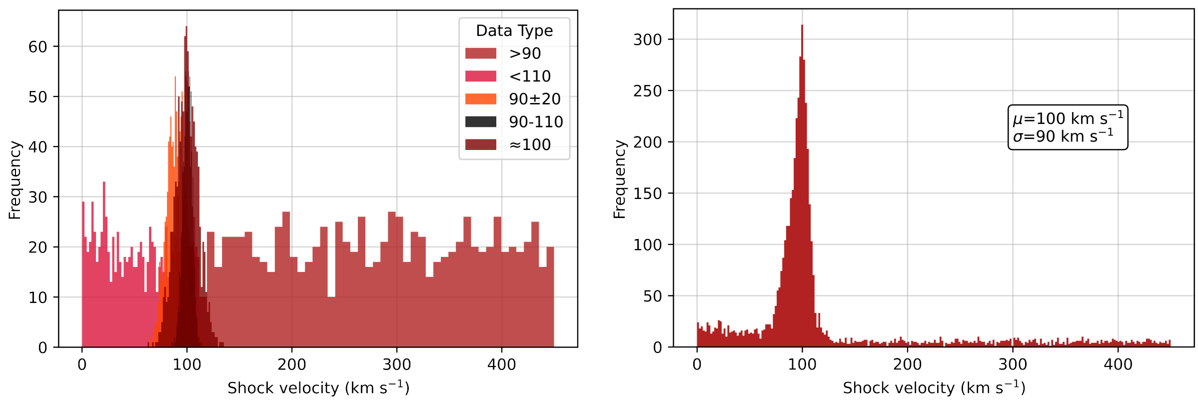

Figure 3.3: Visualisation of the Monte Carlo sampling method used in this work. *Left*: The histograms of Figure 3.2 combined into a single plot. *Right*: Combining the drawn samples for each shock velocity measurement into a single histogram and calculating the median value and standard deviation of the final sample.

4| Results

4.1 Distribution of Physical Parameters

In this section, we present distributions of the physical parameters (electron density and shock velocity) in our sample of SNRs. To get a first image of the scatter in the values, in Figures 4.1 and 4.2 we present multiple electron density and shock velocity measurements per object, for each of the 62 Galactic SNRs we examined. Data in these figures are in their raw form, that is we have not applied the Monte Carlo sampling approach and we have represented upper and lower limits with arrows pointing down and up, respectively. Additionally, errors correspond to those reported in the publications and values lacking errors correspond to data for which errors are not reported in the relevant publications. The measurements in these figures refer to different regions within each remnant or, in the case of shock velocity, different measuring methods used in each case. In Fig. 4.2 data points are color-coded with respect to these methods.

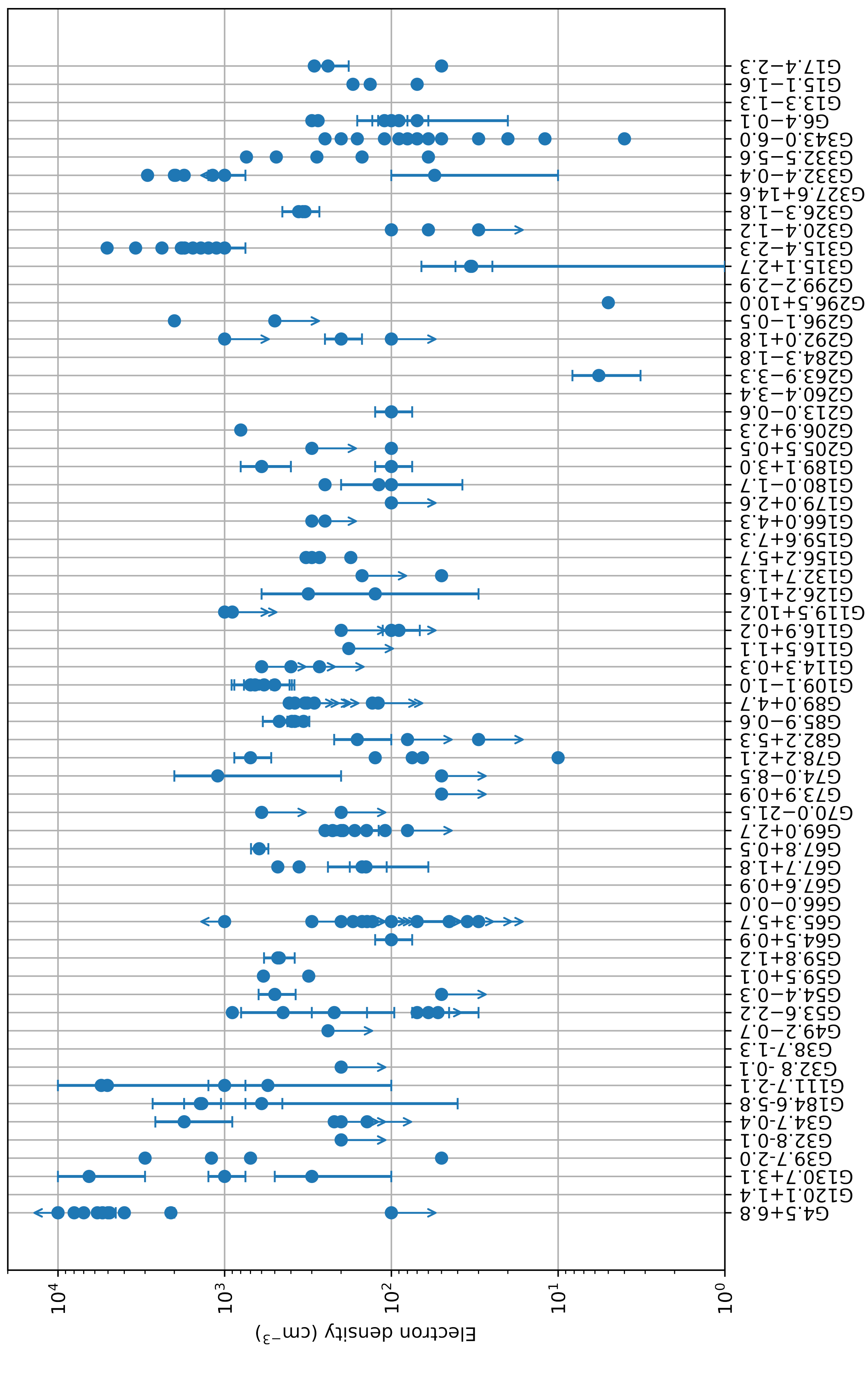

Figure 4.1: Electron density measurements for the different objects in our sample. Each object may have different measurements representing different regions.

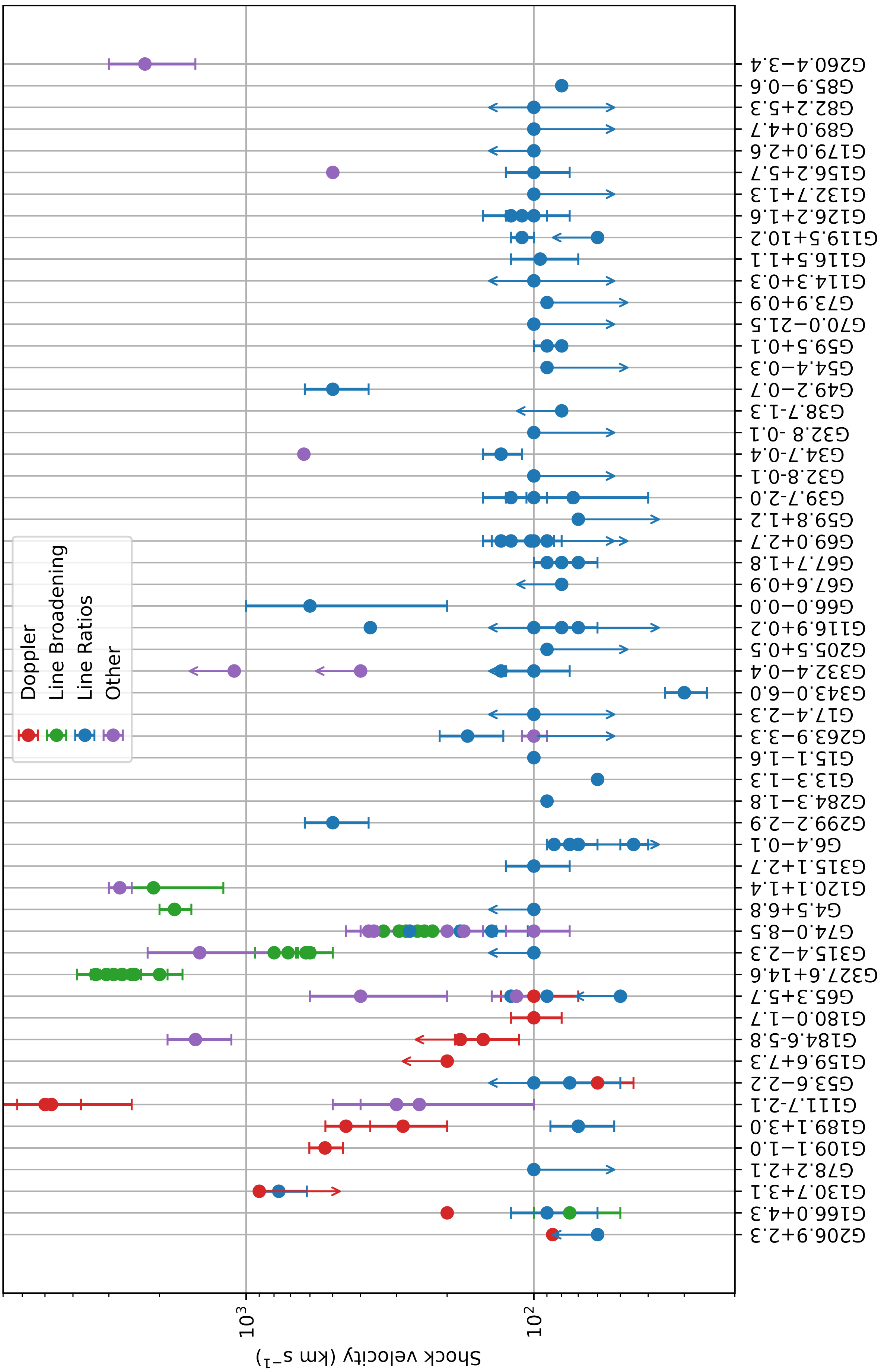

Figure 4.2: Shock velocity measurements for the different objects in our sample, color-coded with respect to the measurement method used. Each object may have different measurements representing different regions.

4.1.1 Individual Objects

We performed a statistical analysis of the measurements within different regions of a given remnant. Here, we consider histograms of remnants with a total of 10 or more electron density and shock velocity measurements across the remnant. Measurements from the same region were averaged, so histogram frequencies add up to the total number of distinct regions observed in each remnant. Additionally, from our literature review [83], we found an object, SN1006, with shock velocity measurements for 133 distinct regions. Unfortunately, not many objects have been studied extensively, so these histograms are not well sampled, yet they still give a first image of the variability of the physical parameters within an object, reflecting the variability of the medium itself surrounding SNR sites. The insights that can be gained from these results are further discussed in Chapter 5.

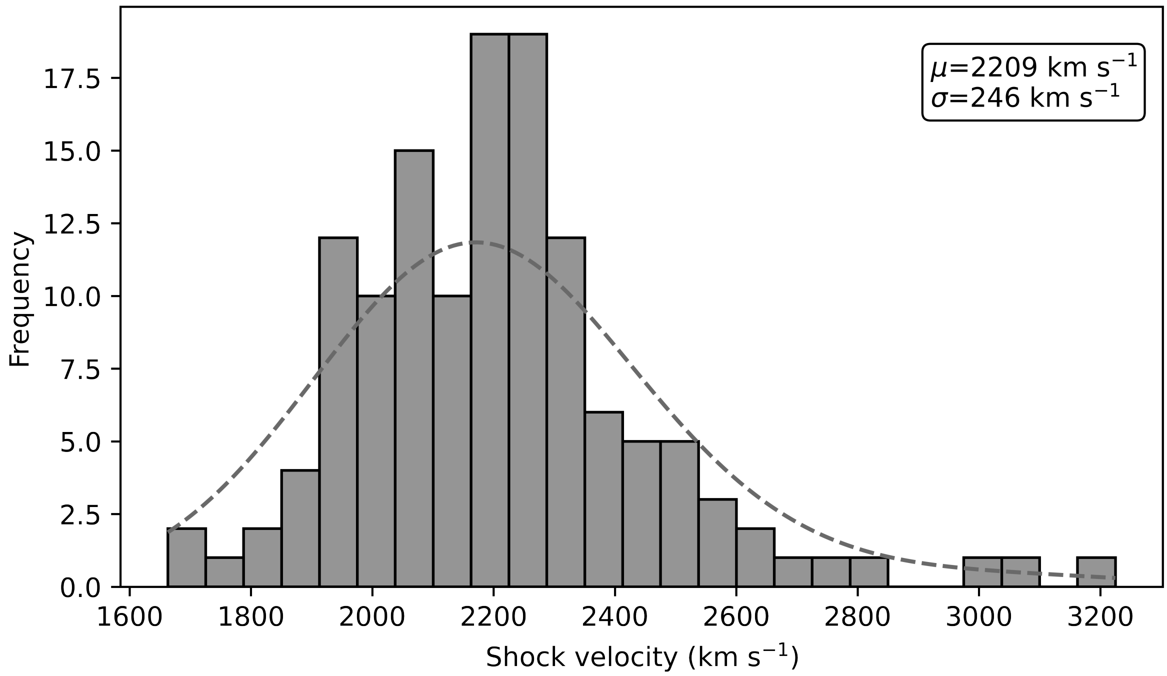

Figure 4.3: The shock velocity distribution within the supernova remnant SN1006 for which we have measurements for 133 distinct regions [83]. All measurements are robust and none are excluded from the statistical analysis.

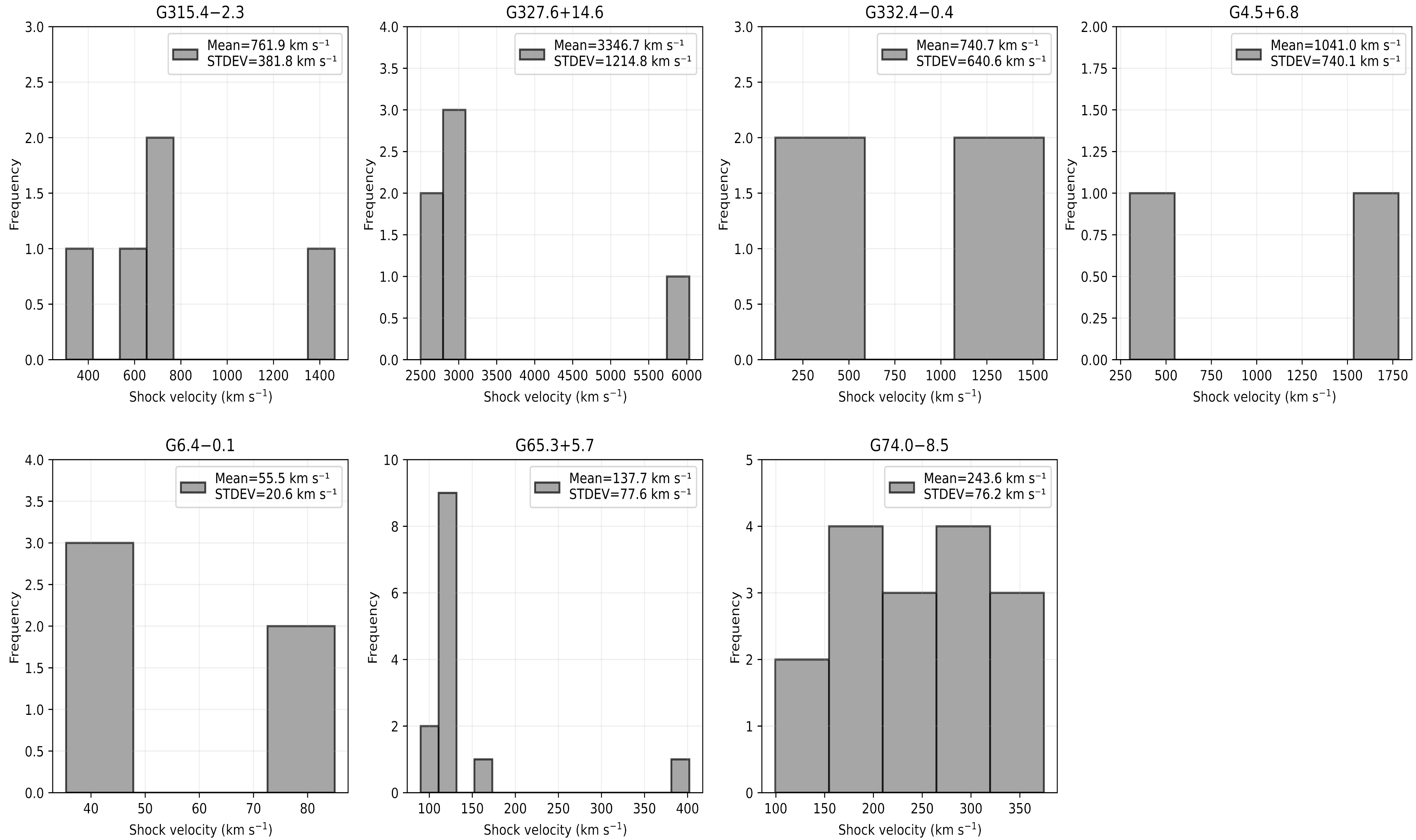

Figure 4.4: The shock velocity distribution within individual objects. Available measurements have been grouped by region of SNR, so frequencies add up to the total number of regions observed in each remnant.

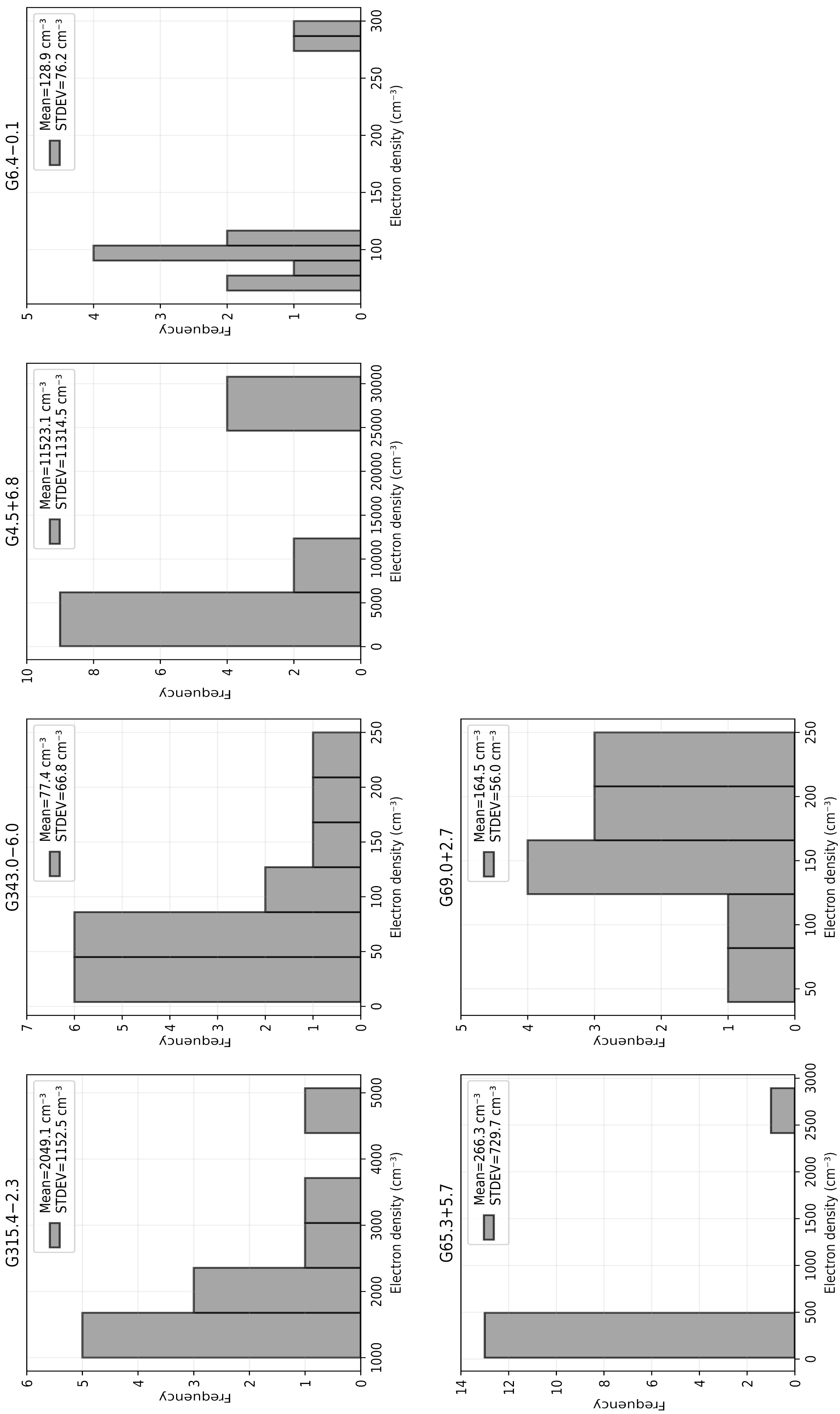

Figure 4.5: The electron density distribution within individual objects. Again, available measurements have been grouped by region of SNR, so frequencies add up to the total number of regions observed in each remnant.

4.1.2 Overall Properties of the SNR Sample

For the entire Galactic SNR sample we studied, we took the mean electron density and shock velocity for each object and we created the histogram of each physical parameter, which can be seen in Figure 4.6. To do this, all available measurements retrieved from publications were grouped by object (regardless of region), according to the methodology described in Chapter 3, to obtain combined mean values for each object. We found that the electron density distribution can be modeled with a log-normal distribution with a mean $\log(n_e) = 2.34$ (cm^{-3}) and a standard deviation of 0.58 (cm^{-3}), whereas the shock velocity distribution with a skew log-normal distribution located at $\log(v_{sh.}) = 1.55$ (km s^{-1}) with a scale of $\omega = 0.88$ and a skewness of $\alpha = 8.57$.

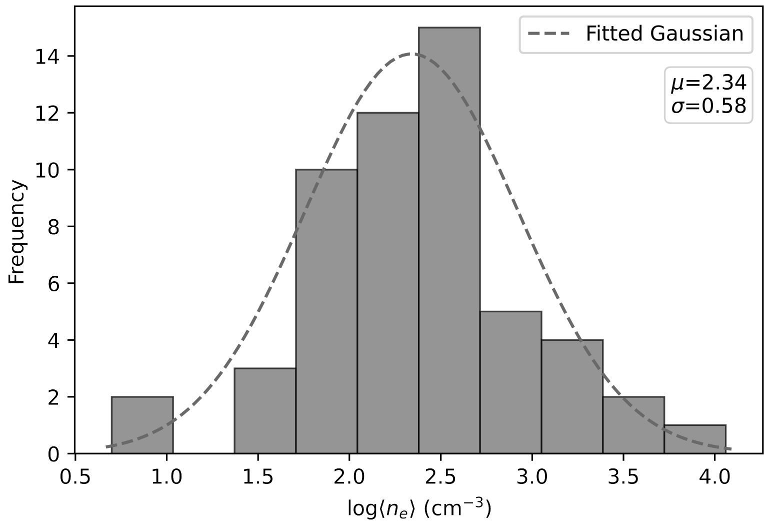

(a) Electron density distribution.

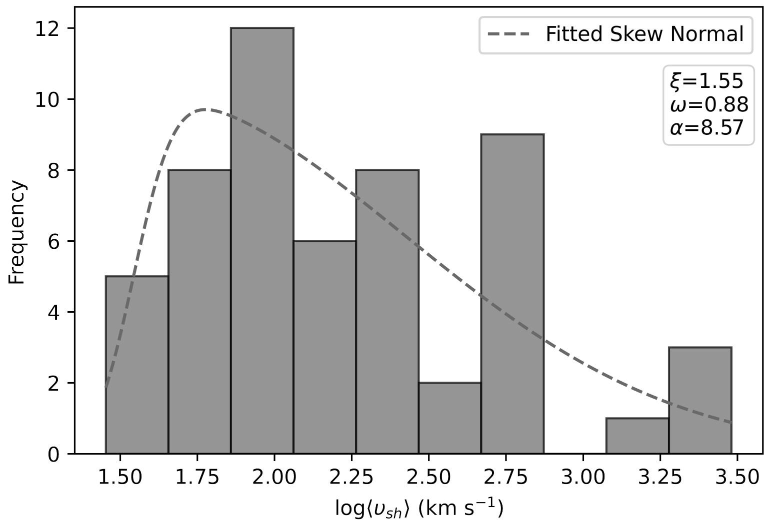

(b) Shock velocity distribution.

Figure 4.6: Physical parameter measurements for the enitre sample of Galactic SNRs. *Top*: The electron density distribution of the population fitted by a log-normal distribution with a mean $\log(n_e) = 2.34$ (cm^{-3}) and a standard deviation of 0.58. *Bottom*: The shock velocity distribution of the population fitted by a skew log-normal distribution located at $\log(v_{sh.}) = 1.55$ (km s^{-1}) with a scale of 0.88 and a skewness of 8.57.

Skewness is a measure of the asymmetry of the distribution about its mean, the location parameter determines the "location" or shift of the distribution and the scale parameter determines its spread. More specifically, the probability density function (PDF) of a skew log-normal distribution with location ξ, scale ω, and parameter α is given by

$$f(x) = \frac{2}{\omega}\phi\left(\frac{x-\xi}{\omega}\right)\Phi\left(\alpha\left(\frac{x-\xi}{\omega}\right)\right), \tag{4.1}$$

where $\phi(x) = \frac{1}{\sqrt{2\pi}}e^{-\frac{x^2}{2}}$ is the standard normal PDF, $\Phi(x) = \int_{-\infty}^{x}\phi(t)dt = \frac{1}{2}\left[1 + erf\left(\frac{x}{\sqrt{2}}\right)\right]$, where "erf" is the error function, is the cumulative distribution function (CDF) and the scale of the x-axis is logarithmic. To obtain the frequency function of the distribution (i.e. the one shown in Figure 4.6b), we denormalize the PDF by multiplying by the histogram bin width and the total number of data points.

4.2 SNR Evolution Model

In Fig. 4.7 we present raw (i.e. unprocessed) shock velocity vs. age data, along with their corresponding errors and upper and lower limits. The points on the plot are color-coded with respect to the common (i.e. decimal) logarithm of the electron density. Grey points represent data lacking a measurement of electron density. The upper right and lower left corners of the plot are vacant, indicating a potential anticorrelation between the shock velocity and age, which is discussed in Chapter 5.

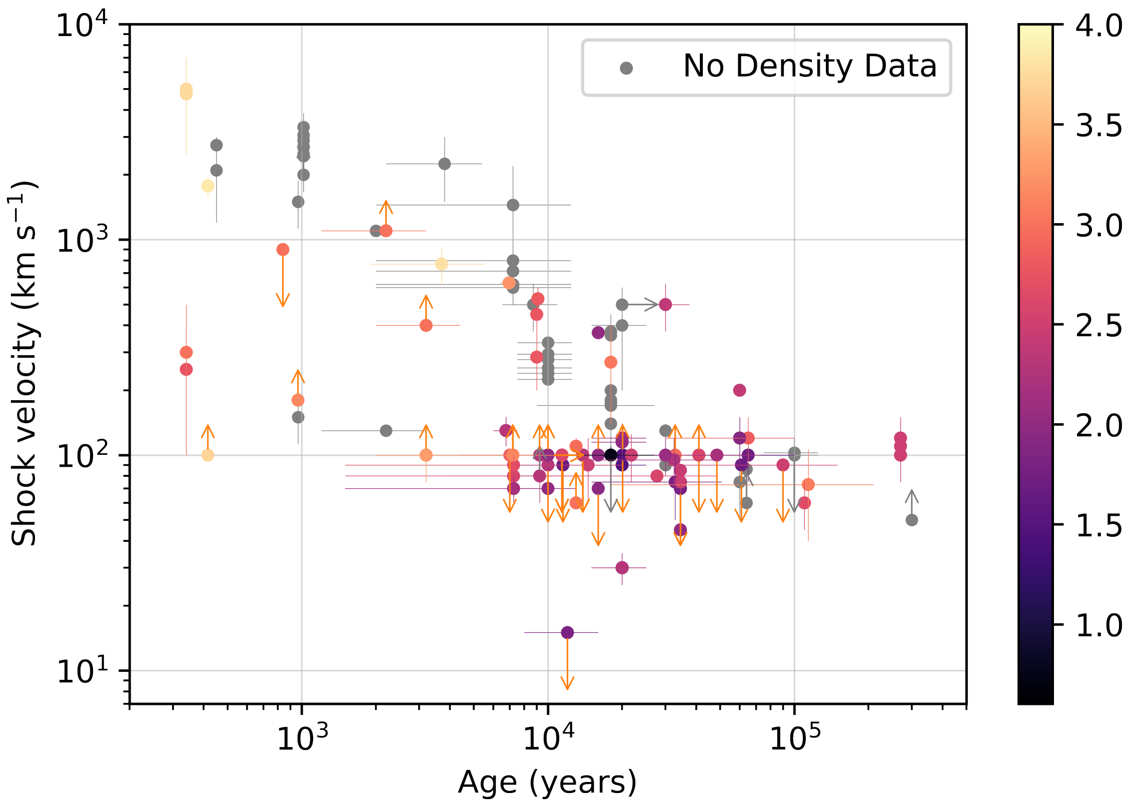

Figure 4.7: The relationship between shock velocity and age in the raw data.

In an attempt to highlight the anticorrelation that seems to be present in Fig. 4.7, we performed our sampling approach described earlier. The result of the synthesis of these data is presented in Figures 4.8 and 4.9. On the left plots of the figures we have taken the mean values of the drawn samples and on the right plots the median values. In Fig. 4.9 we also grouped our drawn samples depending on the velocity measurement methods, as some methods tend to give systematically higher velocities and others lower. The trend is present and it seems that the presence of younger objects in our SNR sample is decisive in its existence. This will be further discussed in Chapter 5.

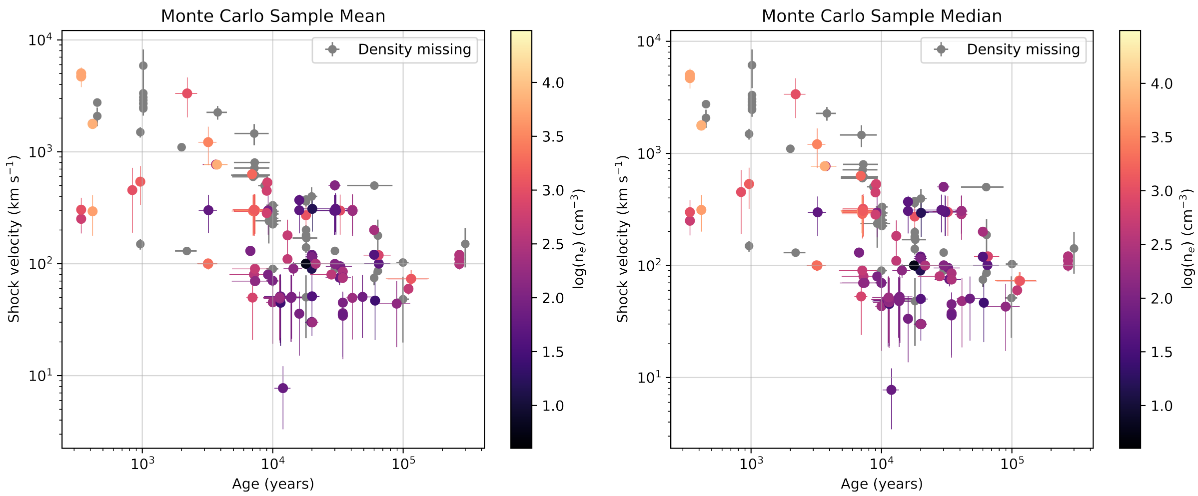

Figure 4.8: The relationship between shock velocity and age. The data have been processed according to a Monte Carlo sampling approach described in the text. On the left plot we have taken the mean value of the samples drawn and on the right the median value. This is the form of the processed data **before** grouping by velocity measurement method.

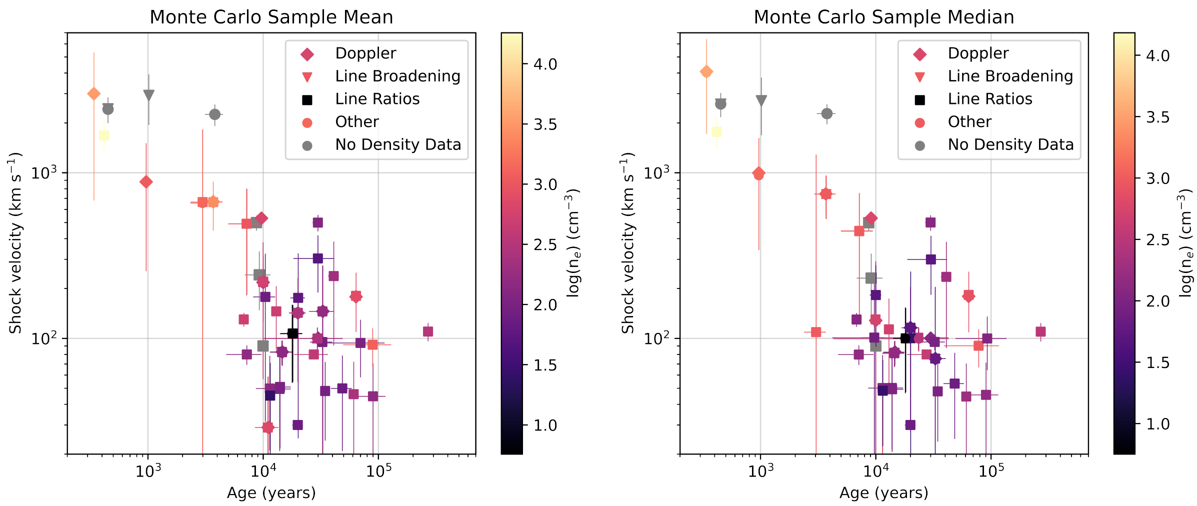

Figure 4.9: The same plot as in Figure 4.8, but for each SNR the samples drawn have been grouped by the method of velocity measurement before performing our statistical analysis.

In Figure 4.10a each point represents a shock velocity measurement for an SNR of a certain age. The measurements are grouped by the method that was used in each case to measure the shock velocity and the data has been processed using the Monte Carlo sampling approach described in Section 3.1. For instance, if we have 5 total velocity measurements for an object, two of which were measured using method A and the rest with method B, the sampling approach as described in Section 3.1 is applied twice, once for method A and once for method B. This leaves us with 2000 combined draws for method A and 3000 combined draws for method B. The calculation of their "aggregated" mean values and standard deviations are used as the final values and errors, respectively, for each method. In the end, we have as many points per object as the number of different velocity measurement methods used in that object; in this case, two points. The points on the plot are color-coded with respect to the logarithm of the average electron density of each SNR.

In order to assess the agreement between the evolutionary model of Cioffi et al. [23] and the data, we superimposed the theoretical curves onto our shock velocity vs. age data. To do this, we took a range of age values ranging from the smallest to the largest age in our dataset and, for distinct values within this range, we check if $t < t_{tr}$, where t_{tr} is the transition time from the Sedov-Taylor to the radiative phase. In this case, the SNR is in the adiabatic phase, so we use eq. 1.3 to get the theoretical shock velocity at that time. Otherwise, the shock velocity is given by the radiative phase equation (Eq. 1.4). These calculations were performed for three different values of ambient/pre-shock density, covering the range of densities in the SNRs. It should be emphasised here that the models use the pre-shock density as opposed to the post-shock density. In cases where the pre-shock density was not reported in our publications, we adopted a correlation wherein the pre-shock density is defined as one-fourth of the post-shock density (the electron density we measure), as imposed by the shock jump conditions, which are a set of physical principles that describe the behavior of a fluid as it encounters a shock front. These conditions are based on the conservation of mass, momentum, and energy. The selection of this relation is relatively inconsequential, as equations 1.1, 1.3, 1.4 and 1.5 governing shock velocity depend on the pre-shock density with small exponents. Thus, variations in the choice of the relation have a limited impact. The results are shown in Figure 4.10a, where the green lines represent the model predictions for the three different ambient densities. More specifically, the nearly vertical lines represent the transition from the adiabatic (Sedov-Taylor) phase of evolution to the radiative phase. Remarkable agreement is observed between the data and the theoretical model.

In Figure 4.10b we show a one-to-one comparison between the data and the model predictions. To create the plot, we grouped our dataset by individual objects and performed the Monte Carlo sampling approach that was described in earlier chapters. Therefore, each data point on the plot represents the average shock velocity measurement for an entire SNR of a certain average age. Additionally, the data points were color-coded with respect to the logarithm of the average density of each SNR, as before. Grey points represent the values predicted by the model of Cioffi et al. based on the age and pre-shock density derived by our sampling approach. Again, we observe a very good agreement.

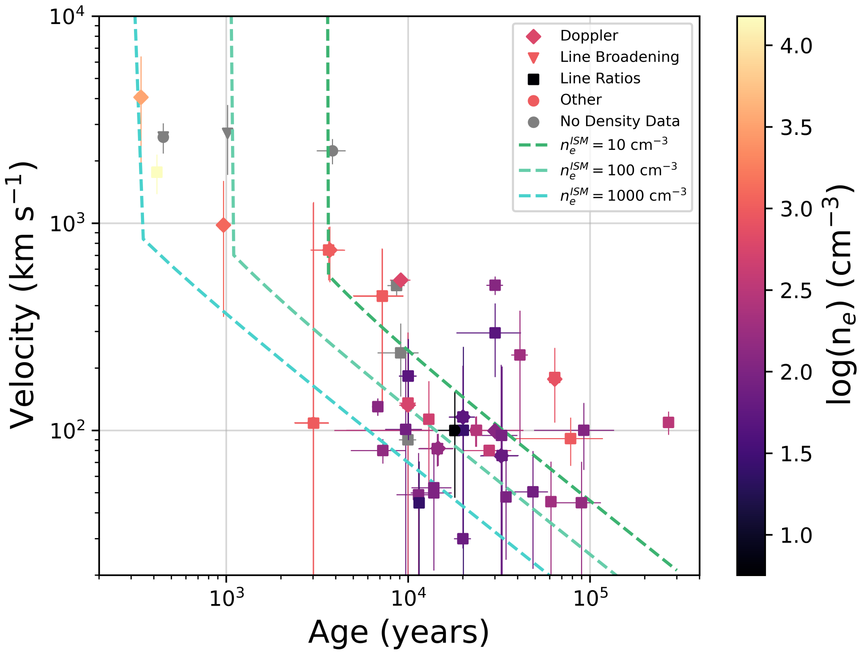

(a) Shock velocity against age and theoretical lines based on the model of Cioffi et al. for different ISM densities.

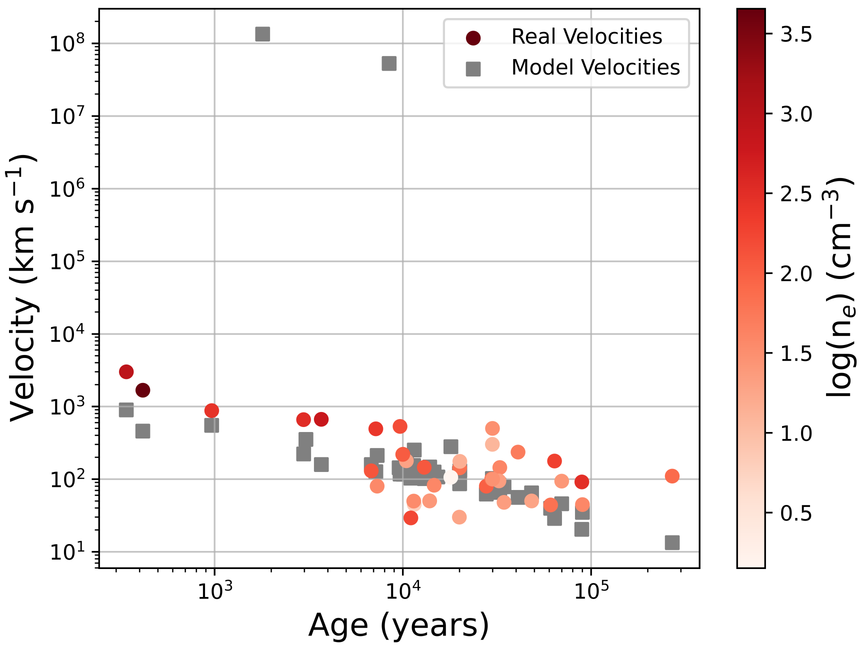

(b) Average shock velocity per object and corresponding model predictions shown with grey points, based on the actual density and age of each object.

Figure 4.10: The measured shock velocity plotted against the SNR age. The lines and grey points correspond to predictions from the SNR evolution models of Cioffi et al. The agreement between the observations and the expected velocities is remarkable.

We also examined the relationship between the shock velocity and electron density in Figure 4.11, where each data point is the mean value for each Galactic SNR. We observe a weak positive trend.

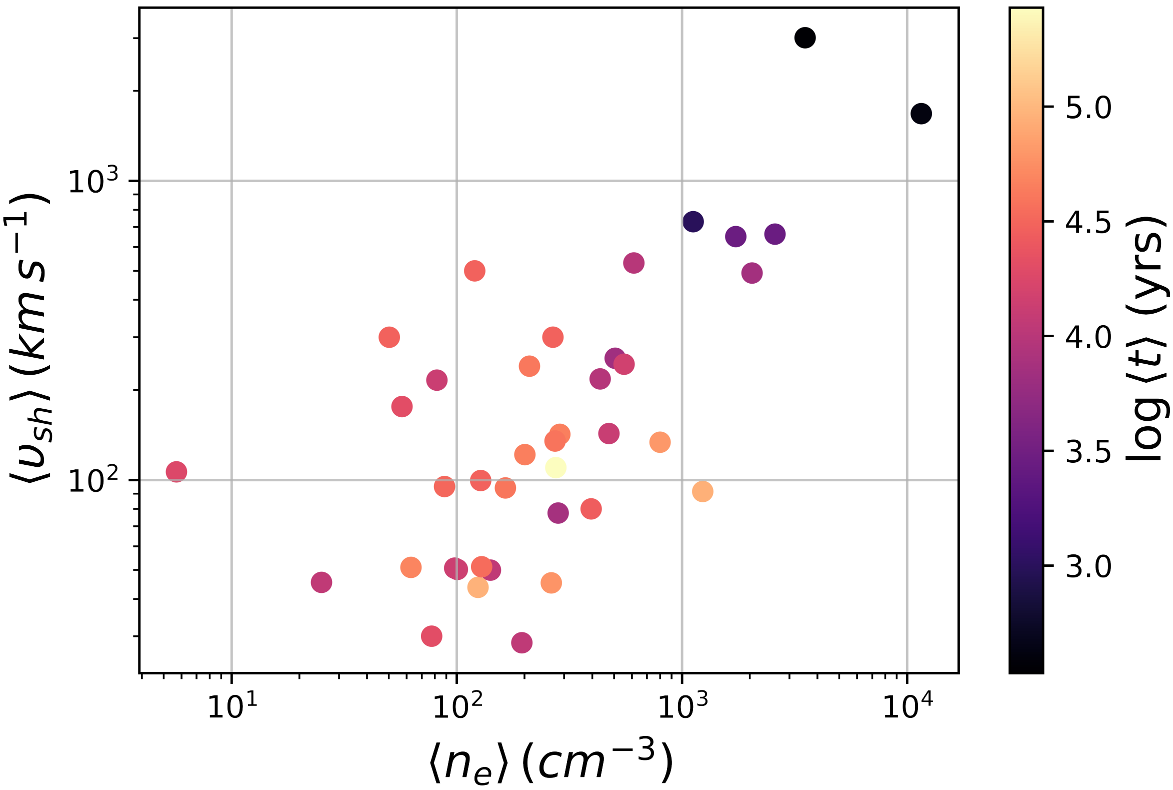

Figure 4.11: The relationship between shock velocity and electron density color-coded with respect to age. A weak positive trend is observed.

5| Discussion

In this chapter we interpret the results of this work. The aim of this project was to provide a picture of the statistics of a sample of 62 supernova remnants in our Galaxy. One of our most important findings is that the electron density follows a log-normal distribution, as can be seen in Fig. 4.6a. This is reasonable, since there's a lower limit to the density set by the density of the interstellar medium and an upper limit associated with the mass of the progenitor star and, therefore, the amount of stellar content being propelled outward into the interstellar medium. At any given time, we have remnants that have only recently exploded and old remnants that have faded out. Observing only one or the other case is statistically improbable. Therefore, most remnants will be somewhere in the middle, their shocks having swept up enough interstellar and circumstellar material, but not having had enough time to dissipate. According to Figure 4.6a this middle point falls at $log(n_e)$=2.34±0.58 (cm^{-3}).

When it comes to the distribution of the shock velocity values across the Galactic population, we expect that since most of the objects we have examined are more than $\sim 10^4$ years old, the shock will have significantly slowed down for most of them. Indeed, this behaviour is also observed in Figure 4.6b, where greater shock velocities are less frequent. This is also expected from the fact that it is statistically improbable for multiple stellar systems to undergo supernova explosions simultaneously, resulting in higher frequency of larger shock velocities. Therefore, we naturally expect the probability density function of the shock velocity to dampen for greater values, as is observed in the skewed log-normal distribution of the shock velocity measurements.

Distributions of physical parameters within individual remnants show significant variability, especially in younger objects. More specifically, we observe that there is significant spread in both electron density and shock velocity across different regions of each remnant, except for a few remnants, namely G6.4-0.1, G65.3+5.7 and G74.0-8.5, which show relatively self-consistent values of shock velocity compared to the rest of the objects for which we have multiple measurements across different regions, as we can see from the small values of standard deviation in Fig. 4.4. This can also be observed in Fig. 4.2, where shock velocity measurements for G6.4-0.1, G65.3+5.7 and G74.0-8.5 are more congregated compared to other objects.

We would expect for the spread of these distributions to be dependent on age, as objects that are older have had more time to interact with the environment surrounding the supernova site, and therefore would be expected to be affected in different ways along different directions of the SNR, following the structure of the ISM and potential neighbouring HII regions and molecular clouds, resulting in greater values of standard deviation. We find that younger objects show significant spread in their physical parameters compared to their older counterparts. This indicates that the effects the immediate surroundings of an SNR have on its evolution are important. The departures from uniformity introduced by the circumstellar and interstellar material immediately surrounding the explosion epicenter seem to be significant. Additionally, older remnants, having had enough time to expand into the ISM seem to incorporate systematically lower density gas. The gradual dissipation of the shock combined with the mixing of the initially clumpy circumstellar material with the more uniform interstellar material implies that the remnant becomes more uniform as it fades out; inhomogeneities encountered in the earlier phases are smoothed out by the passing shock wave, gradually leading up to the dissipation phase.

Finally, for one object, SN1006, we have shock velocity measurements for 133 distinct regions of the remnant. The mean value and standard deviation of these measurements are 2209 km s^{-1} and 246 km s^{-1}, respectively, as can be seen from the corresponding histogram in Figure 4.3. This object can't be correlated to the previous ones, because it outnumbers the number of measurements by one order of magnitude; its shock velocity distribution is much more robust compared to that of the other objects. However, along with the other objects, these distributions do provide valuable constraints for theoretical models of SNR evolution and particle acceleration.

We notice that for most objects in Figures 4.1 and 4.2 shock velocities lie around 100 km s^{-1} and electron densities well below 1000 cm^{-3}. Shock velocities measured via line broadening and Doppler shift tend to be higher, whereas those measured via emission line ratio models yield lower shock velocity values. The first two methods are usually preferred in young X-ray emitting objects, where the shocked gas is heated to millions of degrees and expanding rapidly and, thus, broadening and Doppler effects are significant. This is why these methods are biased in favor of greater shock velocity measurements; shocks are faster in younger objects. However, emission line ratios, particularly those involving emission lines of [O III], [N II] and [S II] are independent of density for density ranges typical of those of the ISM (Allen et al., 2018 [2]), deeming them useful as temperature and, therefore, shock velocity diagnostics for older, cooler objects that have expanded into the ISM. So, for older objects (i.e. the majority of our sample) in which the shock front has expanded into the ISM and therefore slowed down, this method is preferred and therefore consistent with lower values of shock velocity.

The reason why measurements across a single object are not particularly self-consistent is because the departure from uniformity of the ambient medium causes the shock to propagate with different velocity depending on the density of the medium. So, decelerating faster in denser regions of the SNR, such as knotty and filamentary structures, compared to less dense regions. Additionally, if enough time has passed for reverse shocks to be produced by the supernova ejecta catching up with the shock front, they become yet another factor that contributes to the variability of our measurements of shock velocities within an SNR. This is because reverse shocks are less energetic than forward shocks which are powered by the supernova explosion.

Regarding the comparison with the evolutionary models of Cioffi et al., we see that the data avoid the lower left part of the plot in Figure 4.10a, in agreement with the models, while they also follow the downward trend. Additionally, it is expected for young objects to be associated with higher densities, because of the larger density of the circumstellar material, and older objects to be associated with lower densities. This is because older objects have had time to expand into the ISM, which is of much lower density and more uniform than the vicinity of the supernova progenitor system.

Earlier we mentioned that the presence of younger objects in our SNR sample seems to be decisive in the existence of an anti-correlation between shock velocity and age. That is, if we were to remove young objects from our sample, we would not observe a clear anti-correlation between shock velocity and age. Since the dependence on time of the Sedov-Taylor and radiative phases is very similar (see Eq. 1.3 and 1.4), we propose that the main driver for this behavior is the density. More specifically, we theorize that the difference in density between the circumstellar material, which is denser and has a stronger density gradient, and the ISM, which is thinner and smoother, results in faster velocity evolution and a more gradual evolution, respectively. However, there is a wide range of densities, resulting in the scatter we see.

The temporal trajectory of a single object in this plot would start from the upper left edge following a theoretical line of high ambient density and would steadily progress into lines of lower ambient density, as the shock front surpasses the supernova ejecta and circumstellar material and expands into the ISM. The wide range of the ISM densities is reflected in the fact that older objects are spread out over lines of multiple ambient densities.

In Figure 4.11 we observe a weak upward trend of the shock velocity with respect to electron density. We would expect an inversely proportional relation of shock velocity to electron density, as dense environments contribute to the deceleration of the shock. We theorize that the reason behind this trend is the fact that objects in the upper right corner are significantly younger than the rest of the sample, as can be seen from the color bar, and in such objects the shock front has not yet had enough time to decelerate. Furthermore, in these earlier stages the shock front is still interacting with dense regions immediately surrounding the SNR site, such as circumstellar material. This explains why younger objects exhibit greater electron densities *and* shock velocities simultaneously. This further supports the claim that age is the driving factor of shock velocity for optically emitting remnants.

6 | Conclusions

Supernova remnants (SNRs) are the testament of the final act in the life of a massive star. They are important for enriching and heating the interstellar medium, and for providing information on the latest stages of stellar evolution. SNRs are characterized by complex physical processes resulting in a multi-phase gas radiating across the electromagnetic spectrum. Over 300 SNRs are known in our Galaxy, however, so far there have not been any systematic studies of their population (mostly in the optical band). We present an investigation of the physical properties of Galactic SNRs based on an extensive literature survey. We explore the correlations between the physical parameters of SNRs (such as velocit and density) as a function of their age and type, providing for the first time a picture of the overall trends of the properties of the SNR population within our Galaxy.

Our literature survey is based on the Galactic SNR catalogue of Green (2022). We thoroughly examined all available publications of the entire SNR sample focusing on measurements of their shock or expansion velocity, density and temperature, based on a variety of methods and tracers. We found data for 62 SNRs with published information. For 34 objects, we also have information on multiple regions within the SNR, but we only present results for 9 of those with a statistically sufficient number of regions sampled, providing a picture of the variation of the physical parameters within an object. Age and distance information is obtained from the database of high-energy observations of Galactic SNRs (Ferrand & Safi-Harb, 2012). In order to account for upper/lower limits, and value ranges reported in these publications, we followed an approach where we draw values from a Heaviside step function or a Gaussian distribution respectively. We then calculate the mean and standard deviation from these draws. For objects with multiple available measurements, we first calculate the mean of these measurements before including them in our statistical analysis.

We conclude that the density of the SNR population follows a log-normal distribution with a mean $\log(n_e) = 2.34$ (cm^{-3}) and a standard deviation of 0.58. The shock velocity of the population follows a skew log-normal distribution located at $\log(v_{sh.}) = 1.42$ (km s^{-1}), with a skewness of 8.57 and a scale of 0.88. We also explore the relation between shock velocity and density or age. We see that there is no strong correlation between velocity and density. However, there is a clear anticorrelation between velocity and age (as expected from SNR evolution models). This indicates that age is the driving factor of the SNR shock velocity for optically emitting SNRs. Comparison with evolutionary models shows remarkable agreement, affirming the accuracy of our understanding of shock formation and propagation.

The work presented in this study is quite valuable as it offers a first glimpse into the properties of Galactic SNRs as a population, and a systematic comparison with theoretical models. For instance, the statistical distributions of parameters such as density and shock velocity derived here can be used as inputs in theoretical models that can be constructed to predict other parameters, providing a roadmap for understanding the behavior of individual remnants and their collective impact within our Galaxy.

While our study effectively provides a first picture of the overall trends of the properties of the optical SNR population within our Galaxy and supports our current understanding of shock formation and propagation, it should also be noted that this depiction is somewhat rudimentary. The primary challenge we encountered was the scarcity and limited robustness of available data. Notably, temperature data largely relied on theoretical shock models rather than direct measurements, which constrained our ability to explore its correlations with other parameters. As a result, our study refrained from investigating potential relationships between temperature and other SNR characteristics. Additionally, age estimates were often highly uncertain. Future research endeavors should prioritize the construction of a more extensive and precise dataset, complemented by firsthand spectroscopic observations across multiple regions of SNRs. While this approach may demand additional time and resources for deducing physical properties directly from observations, it opens the door to comprehensive cross-correlations involving shock velocity, electron density, temperature, excitation parameters (e.g. emission line ratios), and supernova types. Such investigations could yield valuable insights into the nature of these phenomena, including variations in density and shock velocity associated with different supernova types.

Bibliography/References

[1] Alarie, Alexandre, Bilodeau, Antoine, and Drissen, Laurent. «A hyperspectral view of Cassiopeia A». In: MNRAS 441.4 (July 2014), pp. 2996–3008. DOI: 10.1093/mnras/stu774.

[2] Allen, Mark G. et al. «The MAPPINGS III Library of Fast Radiative Shock Models». In: ApJS 178.1 (Sept. 2008), pp. 20–55. DOI: 10.1086/589652. arXiv: 0805.0204 [astro-ph].

[3] Ambrocio-Cruz, P. et al. «Kinematics of the Galactic Supernova Remnant G206.9+2.3». In: Rev. Mexicana Astron. Astrofis. 50 (Oct. 2014), pp. 323–328.

[4] Baldwin, J. A., Phillips, M. M., and Terlevich, R. «Classification parameters for the emission-line spectra of extragalactic objects.» In: PASP 93 (Feb. 1981), pp. 5–19. DOI: 10.1086/130766.

[5] Blair, W. P. and Kirshner, R. P. «Optical spectrum of the unusual supernova remnant G109.1-1.0». In: Nature 291.5811 (May 1981), pp. 132–133. DOI: 10.1038/291132a0.

[6] Blair, W. P. et al. «The discovery of optical emission from the SNR G126.2 + 1.6». In: ApJ 242 (Dec. 1980), pp. 592–595. DOI: 10.1086/158494.

[7] Blair, W. P. et al. «An optical investigation of the peculiar supernova remnant CTB 80.» In: ApJ 282 (July 1984), pp. 161–171. DOI: 10.1086/162187.

[8] Blair, William P. and Long, Knox S. «New Optical Data on the Supernova Remnant 3C 400.2». In: PASP 100 (Apr. 1988), p. 461. DOI: 10.1086/132192.

[9] Blair, William P., Long, Knox S., and Vancura, Olaf. «A Detailed Optical Study of Kepler's Supernova Remnant». In: ApJ 366 (Jan. 1991), p. 484. DOI: 10.1086/169583.

[10] Bocchino, F. et al. «Multi-wavelength observations and modelling of shock-cloud interaction regions in the Vela Supernova Remnant». In: A&A 359 (July 2000), pp. 316–336.

[11] Bohigas, J. et al. «Spectroscopic observations of supernova remnant candidates W 28, CTB 1, and DR 4.» In: Rev. Mexicana Astron. Astrofis. 8 (Dec. 1983), pp. 155–161.

[12] Bohigas, Joaquı´n, Sauvageot, Jean Luc, and Decourchelle, Anne. «The Warm Interstellar Medium around the Cygnus Loop». In: ApJ 518.1 (June 1999), pp. 324–333. DOI: 10.1086/307247. arXiv: astro-ph/9811333 [astro-ph].

[13] Boumis, P., Mavromatakis, F., and Paleologou, E. V. «First optical light from the supernova remnant G 17.4-2.3». In: A&A 385 (Apr. 2002), pp. 1042–1048. DOI: 10.1051/0004-6361:20020185. arXiv: astro-ph/0201482 [astro-ph].

[14] Boumis, P. et al. «New optical filamentary structures in Pegasus». In: A&A 396 (Dec. 2002), pp. 225–234. DOI: 10.1051/0004-6361:20021365. arXiv: astro-ph/0209258 [astro-ph].

[15] Boumis, P. et al. «The kinematics of the bi-lobal supernova remnant G 65.3+5.7. II..» In: A&A 424 (Sept. 2004), pp. 583–588. DOI: 10.1051/0004-6361:20040410. arXiv: astro-ph/0405350 [astro-ph].

[16] Boumis, P. et al. «Deep optical observations of the supernova remnants G 126.2+1.6, G 59.8+1.2 and G 54.4-0.3». In: A&A 443.1 (Nov. 2005), pp. 175–183. DOI: 10.1051/0004-6361:20053484. arXiv: astro-ph/0508093 [astro-ph].

[17] Boumis, P. et al. «Deep optical observations of the interaction of the SS 433 microquasar jet with the W50 radio continuum shell». In: MNRAS 381.1 (Oct. 2007), pp. 308–318. DOI: 10.1111/j.1365-2966.2007.12276.x. arXiv: 0707.4243 [astro-ph].

[18] Boumis, P. et al. «First optical detection of the supernova remnant G 15.1-1.6». In: A&A 481.3 (Apr. 2008), pp. 705–712. DOI: 10.1051/0004-6361:20079156. arXiv: 0801.3591 [astro-ph].

[19] Boumis, P. et al. «Discovery of optical emission from the supernova remnant G 32.8-0.1 (Kes 78)». In: A&A 499.3 (June 2009), pp. 789–797. DOI: 10.1051/0004-6361/200811474. arXiv: 0903.3124 [astro-ph.GA].

[20] Busser, J. -U., Egger, R., and Aschenbach, B. «G299.2-2.9: a new galactic supernova remnant.» In: A&A 310 (June 1996), pp. L1–L4.

[21] Carter, L. M., Dickel, J. R., and Bomans, D. J. «Expansion of the Supernova Remnant RCW 103». In: PASP 109 (Sept. 1997), pp. 990–997. DOI: 10.1086/133971.

[22] Charlebois, M. et al. «A Hyperspectral View of the Crab Nebula». In: AJ 139.5 (May 2010), pp. 2083–2096. DOI: 10.1088/0004-6256/139/5/2083.

[23] Cioffi, Denis F., McKee, Christopher F., and Bertschinger, Edmund. «Dynamics of Radiative Supernova Remnants». In: ApJ 334 (Nov. 1988), p. 252. DOI: 10.1086/166834.

[24] D'Odorico, S. and Sabbadin, F. «A spectroscopic survey of supernova remnant candidates in the λλ6000-6800 Å spectral region: The observations». In: A&AS 28 (June 1977), p. 439.

[25] Danforth, Charles W., Blair, William P., and Raymond, John C. «A Detailed Analysis of a Cygnus Loop Shock-Cloud Interaction». In: AJ 122.2 (Aug. 2001), pp. 938–953. DOI: 10.1086/321161. arXiv: astro-ph/0104243 [astro-ph].

[26] Dennefeld, M. «The Spectrum of the Supernova Remnant MSH:15-5/6 - G326.3-1.8». In: PASP 92 (Oct. 1980), p. 603. DOI: 10.1086/130719.

[27] Dopita, M. A., Mathewson, D. S., and Ford, V. L. «Optical emission from shock waves. III. Abundances in supernova remnants.» In: ApJ 214 (May 1977), pp. 179–188. DOI: 10.1086/155242.

[28] Dopita, M. A. and Tuohy, I. R. «Spectrophotometry of young supernova remnants.» In: ApJ 282 (July 1984), pp. 135–141. DOI: 10.1086/162184.

[29] Ferrand, Gilles and Safi-Harb, Samar. «A census of high-energy observations of Galactic supernova remnants». In: *Advances in Space Research* 49.9 (May 2012). Online high-energy catalogue of supernova remnants available at http://snrcat.physics.umanitoba.ca/, pp. 1313–1319. DOI: 10.1016/j.asr.2012.02.004. arXiv: 1202.0245 [astro-ph.HE].

[30] Fesen, R. A. «Discovery of large radial velocities in the supernova remnant 3C 58.» In: ApJ 270 (July 1983), pp. L53–L57. DOI: 10.1086/184069.

[31] Fesen, R. A. «The nature of the filaments northeast of the supernova remnant IC 443.» In: ApJ 281 (June 1984), pp. 658–664. DOI: 10.1086/162142.

[32] Fesen, R. A., Blair, W. P., and Kirshner, R. P. «Optical emission-line properties of evolved galactic supernova remnants.» In: ApJ 292 (May 1985), pp. 29–48. DOI: 10.1086/163130.

[33] Fesen, R. A. et al. «The optical emission from the supernova remnant CTA 1.» In: ApJ 247 (July 1981), pp. 148–151. DOI: 10.1086/159021.

[34] Fesen, Robert et al. «Optical Imaging and Spectroscopy of the Galactic Supernova Remnant 3C 58 (G130.7+3.1)». In: ApJS 174.2 (Feb. 2008), pp. 379–395. DOI: 10.1086/522781.

[35] Fesen, Robert A. and Milisavljevic, Dan. «Optical Discovery of an Apparent Galactic Supernova Remnant G159.6+7.3». In: AJ 140.5 (Nov. 2010), pp. 1163–1167. DOI: 10.1088/0004-6256/140/5/1163. arXiv: 1009.0049 [astro-ph.GA].

[36] Fesen, Robert A. et al. «Optical and Radio Emission from the Galactic Supernova Remnant HB 3(G132.6 +1.5)». In: AJ 110 (Dec. 1995), p. 2876. DOI: 10.1086/117736.

[37] Fesen, Robert A. et al. «Optical Imaging and Spectroscopy of the Galactic Supernova Remnants CTB 1 (G116.9+0.2), G116.5+1.1, and G114.3+0.3». In: AJ 113 (Feb. 1997), pp. 767–779. DOI: 10.1086/118297.

[38] Fesen, Robert A. et al. «Ejecta Knot Flickering, Mass Ablation, and Fragmentation in Cassiopeia A». In: ApJ 736.2, 109 (Aug. 2011), p. 109. DOI: 10.1088/0004-637X/736/2/109. arXiv: 1105.3970 [astro-ph.GA].

[39] Fesen, Robert A. et al. «Discovery of an Apparent High Latitude Galactic Supernova Remnant». In: ApJ 812.1, 37 (Oct. 2015), p. 37. DOI: 10.1088/0004-637X/812/1/37. arXiv: 1508.06291 [astro-ph.HE].

[40] Filippenko, Alexei V. «Optical Spectra of Supernovae». In: ARA&A 35 (Jan. 1997), pp. 309–355. DOI: 10.1146/annurev.astro.35.1.309.

[41] Gerardy, Christopher L. and Fesen, Robert A. «Discovery of extensive optical emission associated with the X-ray bright, radio faint Galactic SNR G156.2+5.7». In: MNRAS 376.3 (Apr. 2007), pp. 929–938. DOI: 10.1111/j.1365-2966.2007.11494.x. arXiv: astro-ph/0608522 [astro-ph].

[42] Ghavamian, Parviz et al. «Evidence for Shock Precursors in Tycho's Supernova Remnant». In: ApJ 535.1 (May 2000), pp. 266–274. DOI: 10.1086/308811.

[43] Ghavamian, Parviz et al. «Balmer-dominated Spectra of Nonradiative Shocks in the Cygnus Loop, RCW 86, and Tycho Supernova Remnants». In: ApJ 547.2 (Feb. 2001), pp. 995–1009. DOI: 10.1086/318408. arXiv: astro-ph/0010496 [astro-ph].

[44] Ghavamian, Parviz et al. «The Optical Spectrum of the SN 1006 Supernova Remnant Revisited». In: ApJ 572.2 (June 2002), pp. 888–896. DOI: 10.1086/340437. arXiv: astro-ph/0202487 [astro-ph].

[45] Gök, F. et al. «Optical observations of the galactic supernova remnants G59.5+0.1, G84.9+0.5 and G67.7+1.8». In: Ap&SS 318.3-4 (Dec. 2008), pp. 207–214. DOI: 10.1007/s10509-008-9914-4.

[46] Gök, F. et al. «Optical imaging and spectroscopic observation of the galactic supernova remnant G85.9-0.6». In: Ap&SS 324.1 (Nov. 2009), pp. 17–22. DOI: 10.1007/s10509-009-0150-3. arXiv: 0909.2959 [astro-ph.GA].

[47] Goss, W. M. et al. «Optical identification and spectrum of the supernova remnant G292.0+1.8.» In: MNRAS 188 (Aug. 1979), pp. 357–363. DOI: 10.1093/mnras/188.2.357.

[48] Green, D. A. *A Catalogue of Galactic Supernova Remnants (2022 December version)*. Cavendish Laboratory, Cambridge, United Kingdom. Available at http://www.mrao.cam.ac.uk/surveys/snrs/.

[49] Gull, T. R., Kirshner, R. P., and Parker, R. A. R. «A new optical supernova remnant in Cygnus.» In: ApJ 215 (July 1977), pp. L69–L70. DOI: 10.1086/182480.

[50] Hailey, Charles J. and Craig, William W. «Spectroscopy of the Supernova Remnant CTB 1». In: ApJ 434 (Oct. 1994), p. 635. DOI: 10.1086/174765.

[51] Hartigan, Patrick, Raymond, John, and Hartmann, Lee. «Radiative Bow Shock Models of Herbig-Haro Objects». In: ApJ 316 (May 1987), p. 323. DOI: 10.1086/165204.

[52] Helder, E. A. et al. «Proper motions of Hα filaments in the supernova remnant RCW 86». In: MNRAS 435.2 (Oct. 2013), pp. 910–916. DOI: 10.1093/mnras/stt993. arXiv: 1306.3994 [astro-ph.HE].

[53] Hester, J. J. «The Crab Nebula : an astrophysical chimera.» In: ARA&A 46 (Sept. 2008), pp. 127–155. DOI: 10.1146/annurev.astro.45.051806.110608.

[54] Hester, J. Jeff and Kulkarni, Shrinivas R. «Optical Imagery and Spectrophotometry of CTB 80». In: ApJ 340 (May 1989), p. 362. DOI: 10.1086/167399.

[55] Hester, J. Jeff, Raymond, John C., and Blair, William P. «The Balmer-dominated Northeast Limb of the Cygnus Loop Supernova Remnant». In: ApJ 420 (Jan. 1994), p. 721. DOI: 10.1086/173598.

[56] How, Thomas G. et al. «Optical emission associated with the Galactic supernova remnant G179.0+2.6». In: MNRAS 478.2 (Aug. 2018), pp. 1987–1993. DOI: 10.1093/mnras/sty1007. arXiv: 1804.07403 [astro-ph.HE].

[57] Katsuda, Satoru et al. «Constraining the Age and Distance of the Galactic Supernova Remnant G156.2+5.7 by Hα Expansion Measurements». In: ApJ 826.2, 108 (Aug. 2016), p. 108. DOI: 10.3847/0004-637X/826/2/108. arXiv: 1605.07271 [astro-ph.HE].

[58] Katsuda, Satoru et al. «Spatially Resolved Spectroscopy of a Balmer-dominated Shock in the Cygnus Loop: An Extremely Thin Cosmic-Ray Precursor?» In: ApJ 819.2, L32 (Mar. 2016), p. L32. DOI: 10.3847/2041-8205/819/2/L32. arXiv: 1602.06482 [astro-ph.HE].

[59] Kirshner, Robert, Winkler, P. Frank, and Chevalier, Roger A. «High-Velocity Emission in Young Supernova Remnants: SN 1006 and SN 1572». In: ApJ 315 (Apr. 1987), p. L135. DOI: 10.1086/184875.

[60] Knežević, Sladjana et al. «Balmer Filaments in Tycho's Supernova Remnant: An Interplay between Cosmic-ray and Broad-neutral Precursors». In: ApJ 846.2, 167 (Sept. 2017), p. 167. DOI: 10.3847/1538-4357/aa8323. arXiv: 1708.01605 [astro-ph.HE].

[61] Leibowitz, E. M. and Danziger, I. J. «Spectrophotometry in the galactic supernova remnants RCW 86, 103 and Kepler.» In: MNRAS 204 (July 1983), pp. 273–287. DOI: 10.1093/mnras/204.2.273.

[62] Loll, A. M. et al. «Observations of the Crab Nebula's Asymmetrical Development». In: ApJ 765.2, 152 (Mar. 2013), p. 152. DOI: 10.1088/0004-637X/765/2/152.

[63] Long, Knox S. and Blair, William P. «The Identification of Balmer-dominated Filaments in RCW 86». In: ApJ 358 (July 1990), p. L13. DOI: 10.1086/185768.

[64] Long, Knox S. et al. «W28 and 3C 400.2: Two Shell-like Radio Supernova Remnants with Centrally Peaked X-Ray Morphologies». In: ApJ 373 (June 1991), p. 567. DOI: 10.1086/170076.

[65] Long, Knox S. et al. «Spectroscopy of a Balmer-dominated Filament in the Cygnus Loop with the Hopkins Ultraviolet Telescope». In: ApJ 400 (Nov. 1992), p. 214. DOI: 10.1086/171988.

[66] Longmore, A. J., Clark, D. H., and Murdin, P. «A new optical supernova remnant in Crux.» In: MNRAS 181 (Dec. 1977), pp. 541–546. DOI: 10.1093/mnras/181.3.541.

[67] Lozinskaia, T. A. «The supernova remnants IC 443 and VRO 42.05.01: fast filaments and high-velocity gas.» In: *Australian Journal of Physics* 32 (Mar. 1979), pp. 113–121. DOI: 10.1071/PH790113.

[68] Mavromatakis, F. «Deep optical observations of the supernova remnant G 78.2+2.1». In: A&A 408 (Sept. 2003), pp. 237–243. DOI: 10.1051/0004-6361:20030955.

[69] Mavromatakis, F. «Optical line emission from the supernova remnant G 73.9+0.9». In: A&A 398 (Jan. 2003), pp. 153–158. DOI: 10.1051/0004-6361:20021635.

[70] Mavromatakis, F., Boumis, P., and Goudis, C. D. «The faint supernova remnant G 34.7-0.4 (W44)». In: A&A 405 (July 2003), pp. 591–596. DOI: 10.1051/0004-6361:20030603. arXiv: astro-ph/0305328 [astro-ph].

[71] Mavromatakis, F., Boumis, P., and Paleologou, E. V. «Imaging and spectroscopy of the faint remnant G 114.3+0.3». In: A&A 383 (Mar. 2002), pp. 1011–1017. DOI: 10.1051/0004-6361:20011840. arXiv: astro-ph/0201027 [astro-ph].

[72] Mavromatakis, F., Xilouris, E., and Boumis, P. «The supernova remnant G 6.4-0.1 and its environment». In: A&A 426 (Nov. 2004), pp. 567–575. DOI: 10.1051/0004-6361:20041176.

[73] Mavromatakis, F., Xilouris, E. M., and Boumis, P. «The optical properties of the G89.0+4.7 (HB 21) supernova remnant». In: A&A 461.3 (Jan. 2007), pp. 991–997. DOI: 10.1051/0004-6361:20054786.

[74] Mavromatakis, F. et al. «Optical CCD imaging of the supernova remnant CTA 1». In: A&A 353 (Jan. 2000), pp. 371–379.

[75] Mavromatakis, F. et al. «The peculiar supernova remnant CTB 80». In: A&A 371 (May 2001), pp. 300–311. DOI: 10.1051/0004-6361:20010350. arXiv: astro-ph/0101199 [astro-ph].

[76] Mavromatakis, F. et al. «The supernova remnants G 67.7+1.8, G 31.5-0.6 and G 49.2-0.7». In: A&A 370 (Apr. 2001), pp. 265–272. DOI: 10.1051/0004-6361:20010137. arXiv: astro-ph/0101198 [astro-ph].

[77] Mavromatakis, F. et al. «Deep optical observations of G 65.3+5.7». In: A&A 388 (June 2002), pp. 355–362. DOI: 10.1051/0004-6361:20020511. arXiv: astro-ph/0204079 [astro-ph].

[78] Mavromatakis, F. et al. «Multi-wavelength study of the {G 82.2+5.3} supernova remnant». In: A&A 415 (Mar. 2004), pp. 1051–1063. DOI: 10.1051/0004-6361:20031694. arXiv: astro-ph/0311530 [astro-ph].

[79] Mavromatakis, F. et al. «The faint supernova remnant G 116.5+1.1 and the detection of a new candidate remnant». In: A&A 435.1 (May 2005), pp. 141–149. DOI: 10.1051/0004-6361:20042187. arXiv: astro-ph/0502066 [astro-ph].

[80] Meaburn, J. and Allan, P. M. «Expanding shells in the filamentary edge of the young supernova remnant RCW 103.» In: MNRAS 222 (Oct. 1986), pp. 593–603. DOI: 10.1093/mnras/222.3.593.

[81] Medina, Amber A. et al. «Electron-Ion Equilibrium and Shock Precursors in the Northeast Limb of the Cygnus Loop». In: ApJ 791.1, 30 (Aug. 2014), p. 30. DOI: 10.1088/0004-637X/791/1/30.

[82] Neustadt, Jack M. M., Fesen, Robert A., and Black, Christine S. «Detection of optical emission associated with the Galactic SNR G64.5+0.9». In: MNRAS 469.1 (July 2017), pp. 516–520. DOI: 10.1093/mnras/stx867.

[83] Nikolić, Sladjana et al. «An Integral View of Fast Shocks Around Supernova 1006». In: *Science* 340.6128 (Apr. 2013), pp. 45–48. DOI: 10.1126/science.1228297. arXiv: 1302.4328 [astro-ph.HE].

[84] Osterbrock, Donald E. and Ferland, Gary J. *Astrophysics of gaseous nebulae and active galactic nuclei*. 2006.

[85] Patnaude, Daniel J. and Fesen, Robert A. «A Comparison of X-Ray and Optical Emission in Cassiopeia A». In: ApJ 789.2, 138 (July 2014), p. 138. DOI: 10.1088/0004-637X/789/2/138. arXiv: 1403.5812 [astro-ph.HE].

[86] Paz Arribas, Manuel. «Estimation of trigger rates, data rates and data volumes for CTA and observations of SNR RX J0852.0-4622 with H.E.S.S.» In: (July 2017). DOI: 10.18452/18056.

[87] Pineault, S. et al. «Optical and radio imaging of the supernova remnant VRO 42.05.01 (G 166.0+4.3).» In: A&A 151 (Oct. 1985), pp. 52–60.

[88] Raymond, J. C. et al. «The Preshock Gas of SN 1006 from Hubble Space Telescope Advanced Camera for Surveys Observations». In: ApJ 659.2 (Apr. 2007), pp. 1257–1264. DOI: 10.1086/512483. arXiv: astro-ph/0701311 [astro-ph].

[89] Raymond, J. C. et al. «Ion-Ion Equilibration and Particle Distributions in a 3000 km s^{-1} Shock in SN 1006». In: ApJ 851.1, 12 (Dec. 2017), p. 12. DOI: 10.3847/1538-4357/aa998f.

[90] Raymond, John C. et al. «Non-Maxwellian Hα Profiles in Tycho's Supernova Remnant». In: ApJ 712.2 (Apr. 2010), pp. 901–907. DOI: 10.1088/0004-637X/712/2/901.

[91] Raymond, John C. et al. «Carbon, Helium, and Proton Kinetic Temperatures in a Cygnus Loop Shock Wave». In: ApJ 805.2, 152 (June 2015), p. 152. DOI: 10.1088/0004-637X/805/2/152. arXiv: 1504.01423 [astro-ph.GA].

[92] Ren, Juan-Juan et al. «Mapping the emission line strengths and kinematics of supernova remnant S147 with extensive LAMOST spectroscopic observations». In: *Research in Astronomy and Astrophysics* 18.9, 111 (Aug. 2018), p. 111. DOI: 10.1088/1674-4527/18/9/111. arXiv: 1804.10989 [astro-ph.GA].

[93] Rho, Jeonghee et al. «An X-Ray and Optical Study of the Supernova Remnant W44». In: ApJ 430 (Aug. 1994), p. 757. DOI: 10.1086/174446.

[94] Rosado, M. «Kinematics of the supernova remnant G65.2 plus 5.7 in Cygnus». In: ApJ 250 (Nov. 1981), pp. 222–226. DOI: 10.1086/159365.

[95] Rosado, M. «Optical Emission from the Supernova Remnants G126.2+1.6 G206.9+2.3 and CTB13». In: Rev. Mexicana Astron. Astrofis. 5.3 (July 1982), p. 127.

[96] Rosado, M. «The optical emission of the SNR 3C 400.2.» In: Rev. Mexicana Astron. Astrofis. 8 (June 1983), pp. 59–62.

[97] Ruiz, M. T. «Spectrophotometry of the optical emission from RCW 103 and Milne 23.» In: AJ 88 (Aug. 1983), pp. 1210–1221. DOI: 10.1086/113411.

[98] Ruiz, Maria Teresa and May, Jorge. «MSH 10-53: A Supernova Remnant Interacting with Molecular Clouds». In: ApJ 309 (Oct. 1986), p. 667. DOI: 10.1086/164634.

[99] Sabbadin, F. «Spectroscopic observations of filamentary nebulae in the Cygnus X region.» In: A&A 51 (Aug. 1976), pp. 159–162.

[100] Sabbadin, F. and D'Odorico, S. «Spectroscopic observations of the supernova remnant candidates 3C 400.2 and S91.» In: A&A 49 (May 1976), pp. 119–123.

[101] Sabin, L. et al. «New Galactic supernova remnants discovered with IPHAS». In: MNRAS 431.1 (May 2013), pp. 279–291. DOI: 10.1093/mnras/stt160. arXiv: 1301.6416 [astro-ph.SR].

[102] Sánchez-Cruces, M. et al. «Kinematics of the Galactic Supernova Remnant G109.1-1.0 (CTB 109)». In: MNRAS 473.2 (Jan. 2018), pp. 1705–1717. DOI: 10.1093/mnras/stx2460. arXiv: 1709.07986 [astro-ph.GA].

[103] Sankrit, Ravi, Blair, William P., and Raymond, John C. «Optical and Far-Ultraviolet Spectroscopy of Knot D in the Vela Supernova Remnant». In: ApJ 589.1 (May 2003), pp. 242–252. DOI: 10.1086/374591. arXiv: astro-ph/0302152 [astro-ph].

[104] Seward, F. D. et al. «A ROSAT-detected, New Galactic Supernova Remnant in Sagittarius, G13.3-1.3». In: ApJ 449 (Aug. 1995), p. 681. DOI: 10.1086/176089.

[105] Sollerman, J. et al. «High resolution spectroscopy of Balmer-dominated shocks in the RCW 86, Kepler and SN 1006 supernova remnants». In: A&A 407 (Aug. 2003), pp. 249–257. DOI: 10.1051/0004-6361:20030839. arXiv: astro-ph/0306196 [astro-ph].

[106] Stupar, M. and Parker, Q. A. «Optical detection and spectroscopic confirmation of supernova remnant G213.0-0.6 (now redesignated as G213.3-0.4)». In: MNRAS 419.2 (Jan. 2012), pp. 1413–1420. DOI: 10.1111/j.1365-2966.2011.19797.x. arXiv: 1110.1827 [astro-ph.GA].

[107] Stupar, M., Parker, Q. A., and Filipović, M. D. «G315.1+2.7: a new Galactic supernova remnant from the AAO/UKST Hα survey». In: MNRAS 374.4 (Feb. 2007), pp. 1441–1448. DOI: 10.1111/j.1365-2966.2006.11248.x. arXiv: astro-ph/0612771 [astro-ph].

[108] Stupar, M. et al. «Multiwavelength study of a new Galactic SNR G332.5-5.6». In: MNRAS 381.1 (Oct. 2007), pp. 377–388. DOI: 10.1111/j.1365-2966.2007.12296.x. arXiv: 0708.0615 [astro-ph].

[109] Sutherland, Ralph S. and Dopita, Michael A. «Young Oxygen-rich Supernova Remnants. I. Observations of Three Southern Remnants». In: ApJ 439 (Jan. 1995), p. 365. DOI: 10.1086/175180.

[110] Walker, A. J. and Zealey, W. J. «Multifibre spectroscopy of the supernova remnant candidate RCW 114». In: MNRAS 325.1 (July 2001), pp. 287–292. DOI: 10.1046/j.1365-8711.2001.04423.x.

[111] Whitehead, M. J., Meaburn, J., and Clayton, C. A. «Optical observations of the morphology and kinematics of the compact core of the peculiar supernova remnant CTB 80.» In: MNRAS 237 (Apr. 1989), pp. 1109–1125. DOI: 10.1093/mnras/237.4.1109.

[112] Winkler, P. F., Olinger, Todd M., and Westerbeke, Scott A. «CCD Mosaic Images of the Supernova Remnant 3C 400.2». In: ApJ 405 (Mar. 1993), p. 608. DOI: 10.1086/172392.

[113] Winkler, P. Frank and Long, Knox S. «Far-Flung Filaments of Ejecta in the Young Supernova Remnant G292.0+1.8». In: AJ 132.1 (July 2006), pp. 360–370. DOI: 10.1086/505042. arXiv: astro-ph/0512078 [astro-ph].

[114] Zealey, W. J., Dopita, M. A., and Malin, D. F. «The interaction between the relativistic jets of SS433 and the interstellar medium». In: MNRAS 192 (Sept. 1980), pp. 731–743. DOI: 10.1093/mnras/192.4.731.